Shock waves in star- and planet-forming regions

青田，拓大

(Degree)
博士（理学）

(Date of Degree)
2014-03-25

(Date of Publication)
2015-03-25

(Resource Type)
doctoral thesis

(Report Number)
甲第6126号

(URL)
https://hdl.handle.net/20.500.14094/D1006126

-博士学位論文-

Shock waves in star- and planet-forming regions
星・惑星形成領域における衝撃波

専攻名 地球惑星科学専攻
学籍番号 098s401s
氏名 青田拓大
神戸大学大学院理学研究科博士課程後期課程

2014 年 1 月 提出

Contents

Introduction of this thesis

Overview of interstellar shocks

In interstellar space, supersonic flows are ubiquitous, e.g. supernova explosions, accretion onto protostars and protoplanetary disks, and outflows from young stellar object. Deceleration of the supersonic flow to subsonic flow is accompanied by shock waves. The gas is compressed, and the kinetic energy of the bulk motion is transformed to thermal energy. If the gas is adiabatic, temperature in the post shock gas (T_1) is given by Rankin-Ugonio equation (Landau & Lifshitz 1987; Zel'dovich & Raizer 2002)

$$\frac{T_1}{T_0} = \frac{[2\gamma M^2 - (\gamma - 1)][(\gamma - 1)M^2 + 2]}{(\gamma + 1)^2 M^2},$$

where T_0, M and γ are gas temperature of pre-shock gas, Mach number, and ratio of specific heat. With typical cloud temperature (10 K in molecular clouds) and flow velocity of molecular cloud 5km/s, typical turbulent velocity in molecular clouds, the post shock temperature is as high as 1000 K. Such high temperature could alter their chemical composition of the gas, allowing reactions with activation barrier to proceed. Thus shock waves are important for both physical and chemical evolution of the interstellar medium (ISM).

The interstellar shocks are however, not adiabatic. The post-shock gas is cooled by radiation of molecules, atoms, and ions. It should be noted that these lines of coolants determine the gas temperature, and thus affect the gas pressure and dynamics. The abundances of the coolants, on the other hand, are determined by chemical reactions, the rate of which depends on the temperature. Coupling of hydrodynamics and microscopic processes (chemical reactions and line emissions) is thus essential. For example, Draine et al. (1983) calculated the low and mid velocity ($5 \sim 50$ km/s) shock structure and showed that H_2O

is formed by the following reactions

$$H_2 + O \rightarrow OH + H$$

$$OH + H_2 \rightarrow H_2O + H,$$

and rotational lines of H_2O become the main coolant of shock heated gas. These reactions have activation barrier, and thus proceed only at temperature of > 300 K.

Many authors have studied the interstellar shock since early times. The shock structure can be divided into four distinct regions in non-magnetic shocks (figure 1); (a) radiative precursor in which supersonic gas is heated by photons emitted by shocked gas (especially in fast shocks) (b) thin adiabatic shock front (c) post-shock region where the now subsonic gas cools by the line emission. (d) molecular formation region where ions recombine, and molecules reform. On the other hand, Draine (1980) discussed the magnetic effect in shocked region. He showed that magnetosonic waves propagate *ahead* of the shock front, and as a result, the density and temperature distributions become continuous. It is called C-shock. Interstellar shocks are observed via highly excited lines and lines of molecules which can be abundant in the shock. Several theoretical works focus on the formation of the molecules and the intensity of rotational and vibrational lines of molecules (e.g. H_2, SiO, H_2O) from shock region (e.g. Iglesias & Silk 1978; Draine et al. 1983; Hollenbach & McKee 1989; Neufeld & Dalgarno 1989; Neufeld & Hollenbach 1994; Hassel et al. 2010; Flower & Pineau des Forets 2010), and showed that the lines of H_2, SiO, and H_2O can be used as the shock tracers. Grain surface species are desorbed to the gas phase via sputtering and thermal desorption in the shock, and thus can be used as shock tracers (e.g. Draine & Salpeter 1979; Draine et al. 1983; Neufeld & Hollenbach 1994; Jiménez-Serra et al. 2008; see also chapter 3).

Shocks in star formation

Shock waves play the important roles in star formation. Figure 2 shows the schematic picture of the star- and planet forming processes.

Molecular clouds are formed by a collision of diffuse gas (stage 1). The post shock gas is efficiently cooled to be dense cold gas. When the gas column density becomes sufficiently

high to shield interstellar UV radiation, gas is transformed to molecules (stage 2), typical timescale of which is several Myrs − 10 Myrs (e.g. Bergin et al. 2004; Glover & Mac Low 2007b; Glover et al. 2010; Clark et al. 2012; Inoue & Inutsuka 2012). Koyama & Inutsuka (2002) showed that the post-shock gas is thermally unstable. Small clumps of dense gas are produced by the thermal instability (see also Inoue & Inutsuka 2008, 2012), which coincide with the tiny (∼100AU) structure observed in HI clouds (e.g. Heiles 1997; Sakamoto & Sunada 2003). The clumps float in the warm gas with velocity dispersion, which can account for the large velocity dispersion in molecular clouds (e.g. Larson 1981; Fukui et al. 2008). Although the velocity dispersion is supersonic for cold dense gas, it is subsonic in warm gas and thus does not dissipate.

Star formation starts in the molecular cloud core triggered by the gravitational collapse (stage 3). As a result, protostar and protoplanetary disk are formed (stage 4). Outflow from the protostar collides with ambient gas. In the outflow shocks, a fraction of the grain surface species could be desorbed to the gas phase via sputtering and/or heating of dust in the shock wave (e.g. Draine & Salpeter 1979; Lunine et al. 1991; Neufeld & Hollenbach 1994). For example, SiO, H_2O, and complex organic molecules (e.g. $HCOOCH_3$, CH_3OH) are detected in shocked region (e.g. Mikami et al. 1992; Jiménez-Serra et al. 2004; Nisini et al. 2010; Sugimura et al. 2011). Because grain surface species cannot be observed directly due to low temperature in molecular clouds, it is important to observe the outflow shock region to understand the composition of interstellar grain.

Accretion shocks occur at the disk surface, as well, since the contraction of protostellar envelope is supersonic. Desorption and chemical reactions in the shock heated gas change the chemical composition of dust and gas, which are raw material for planetary system formation (e.g. Lunine et al. 1991; Neufeld & Hollenbach 1994; Ilee et al. 2011). In recent years, theoretical models of chemistry in protostellar cores and forming disks have been constructed by several groups (e.g. Rodgers & Charnley 2003; Aikawa et al. 2008, 2012; Visser et al. 2009, 2011). For example, Visser et al. (2009, 2011) showed that the chemical composition of the infalling fluid parcel depends on its trajectory. If the fluid parcel experiences only low temperatures, a significant amount of interstellar ice can survive to reach the disk. Desorption via accretion shock, however, is not considered in these papers.

In my doctor thesis, I investigate shock waves in various stages in star formation (Figure 2). In chapter 1, I study the effect of thermal instability in shock heated HI and molecular cloud (red square in Figure 2). While the thermal instability in the shocked warm HI gas is investigated in the context of cloud formation, it is not studied in cold HI gas (cold neutral medium) and molecular gas. Since shocks occur in molecular clouds as well, detailed study on the effect of thermal instability in the shocked molecular clouds must be explored. In this work, I study the thermal stability in shocked CNM and molecular cloud using 1D MHD code including detail chemical reaction network.

In chapter 2, I study the chemical evolution of the shocked region created by the collision between an outflow gas and ambient molecular clouds (green square in Figure 2). In this work, I focus on the Phosphorous bearing species. Phosphorous species is very rare in interstellar space; only 6 species are detected in interstellar space. The abundances of the observed P-bearing species ($10^{-9} \sim 10^{-8}$) relative to hydrogen are much smaller than the solar abundance of phosphorus (10^{-7}). Detection of P-bearingg species are limited to the envelopes of evolved stars (e.g. IRC+10216), except for PN (Phosphine-nitrogen), which is found in high mass star forming region (e.g. Turner & Bally 1987). Recently, Yamaguchi et al. (2011) detected PN in a low mass star-forming region, L1157 B1, for the first time. In this work, I investigate how PN is formed in the shocked gas, and how the PN abundance depends on the molecular abundances of the pre-shock gas and ice.

In chapter 3, I study sputtering and thermal desorption of grain-surface species in protoplanetary disks (blue square in Figure 2). While Neufeld & Hollenbach (1994) investigated evaporation of ices in accretion shock onto the disk, sputtering was not considered. Sputtering of grain-surface species have been investigated in interstelalr shocks, but the density ($> 10^6$ cm^{-3}) and velocity range relevant for the disk have not been covered by previous work. I investigate the fraction of H_2O, SO, CO_2, and CH_4 desorbed to the gas phase via sputtering and thermal desorption in shocks with various parameter sets relevant for protoplanetary disks.

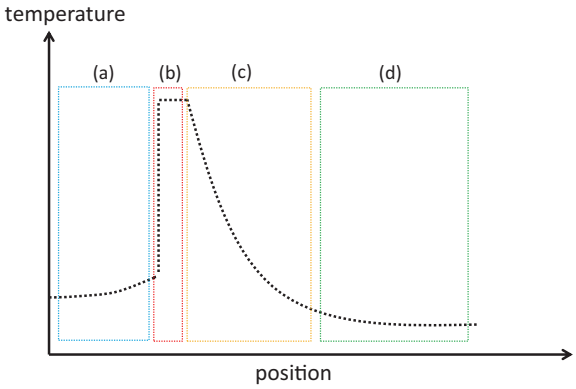

Figure 1: Schematic picture of the shock structure (cf. Neufeld & Dalgarno 1989). (a) radiative precursor in which supersonic gas is heated by photons emitted by shocked gas (especially in fast shocks). (b) thin adiabatic shock front. (c) post-shock region where the now subsonic gas cools by the line emission. (d) molecular formation region where ions recombine, and molecules reform.

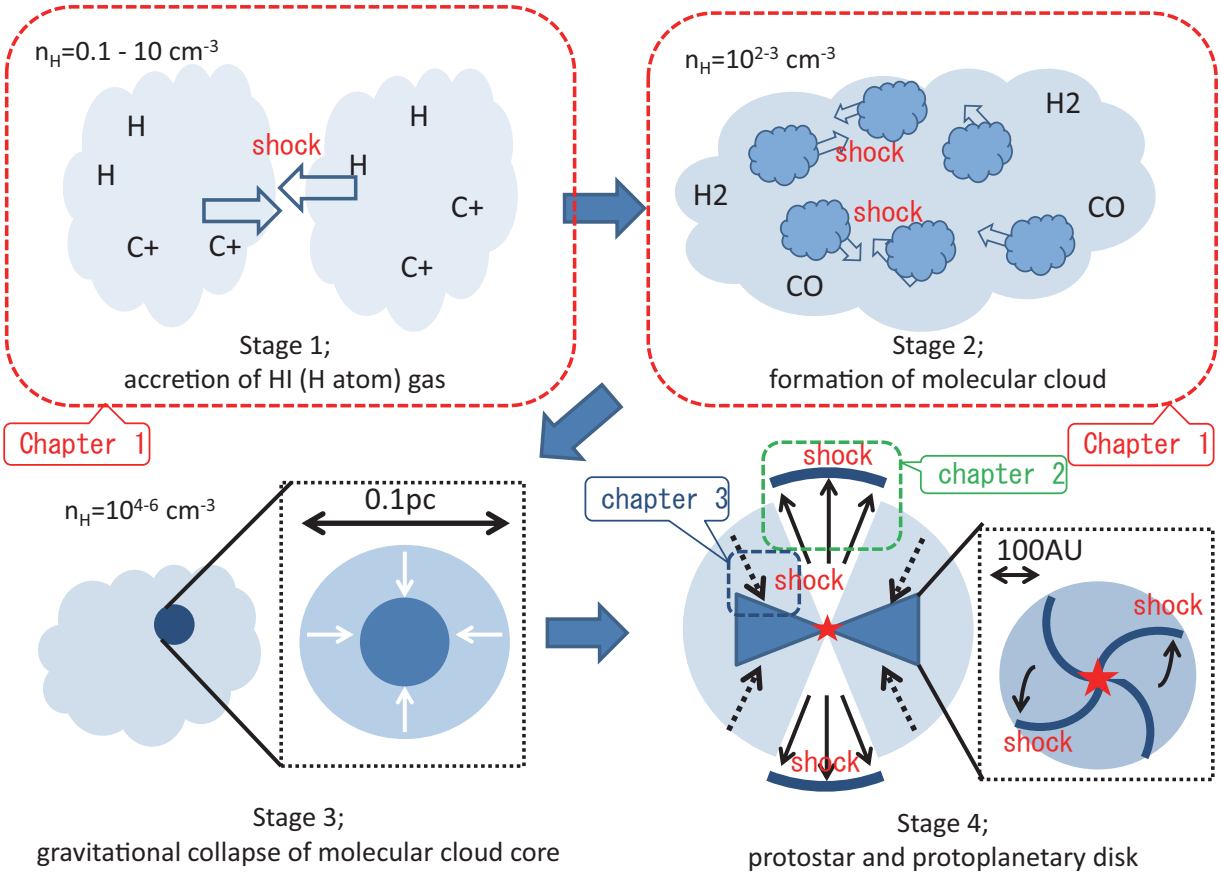

Figure 2: Schematic picture of the star- and planet forming processes. Shock waves occur in every situation. In Chapter 1, I focus on HI and molecular clouds. In Chapter 2, I focus on outflow shocks. In Chapter 3, I focus on accretion shocks on the protoplanetary disk.

Chapter 1

Thermal Instability behind a Shock Wave in HI and Molecular Clouds [1]

1.1 Introduction

Thermal instability is an important physical process to determine the structure in the interstellar medium (Field 1965). It is well established that the neutral gas in the interstellar medium (ISM) consists of two distinct phases: cold neutral medium (CNM) and warm neutral medium (WNM) (Field et al. 1969; Wolfire et al. 1995; Heiles & Troland 2003). Field et al. (1969) calculated the thermal equilibrium state in ISM considering the cosmic ray heating and line cooling by H, O, and C[II]. They showed that there are three physical states under the pressure equilibrium: two stable states and one unstable state. The stable states correspond to the CNM and the WNM. When the WNM transforms to the CNM in converging flows and/or shocks, the gas goes through a thermally unstable state (Hennebelle & Pérault 1999; Koyama & Inutsuka 2000; Heitsch et al. 2005; Vázquez-Semadeni et al. 2006).

Many authors have studied the dynamical condensation and fragmentation processes of the ISM driven by the thermal instability in the shock in WNM. Koyama & Inutsuka (2000); Koyama & Inutsuka (2002) showed that small-scale clumps of CNM are formed behind the shock front in WNM (see also, Hennebelle & Pérault 1999; Hennebelle & Audit 2007; Inoue & Inutsuka 2008, 2009; Heitsch et al. 2008; Vázquez-Semadeni et al. 2007). Koyama & Inutsuka (2000) also investigated the shock propagation *within* the CNM, and

found that the shocked layer in the CNM is thermally unstable, as well. More recently, Inoue & Inutsuka (2012) has succeeded in forming very turbulent molecular clouds by accretion of CNM mixed with WNM.

The thermal instability works as follows. Consider an isobaric gas with small density perturbation. If the gas in small density enhancement (i.e. temperature decline) has a larger cooling rate than the surrounding gas, the density enhancement grows. In other words, the condition is determined by how the cooling rate depends on the density and temperature. Thermal instability thus could occur in denser regions like molecular clouds as well, and has actually been studied. de Jong et al. (1980) investigated the thermal-chemical instability (e.g. Glassgold & Langer 1976) in the chemical transition region where the dominant form of carbon changes from C[II] to CO (Glassgold & Langer 1975), and showed that the thermal-chemical instability is not active. Gilden (1984) investigated thermal instability in molecular clouds with density $n \sim 10^3$ cm^{-3} and temperature $T \simeq 35$ - 75 K, and found that such a cloud is thermally unstable. Nejad-Asghar (2007, 2011) investigated thermal instability in molecular cloud cores ($n \sim 10^5 - 10^6$ cm^{-3}) with the effect of the ambipolar diffusion, and showed that the thermal instability can grow in quasi-magnetohydrostatic, self-gravitating slab (Nejad-Asghar 2007) and axisymmetric cylindrical core (Nejad-Asghar 2011).

On the other hand, to our best knowledge, the role of thermal instability in shock heated molecular clouds has not yet been studied. Molecular clouds are characterized by supersonic velocity dispersions, which are most probably due to turbulence (e.g. Larson 1981; Solomon et al. 1987). Dissipation of the supersonic turbulence would be accompanied by shocks. Shock waves are also driven by collisions of protostellar outflows with ambient gas.

Molecular clouds are known to have clumpy structures. While many of the clumps are gravitationally bound, there are very small-scale structures as well: a size of $\sim$1000AU and density of $n \simeq 10^4$ cm^{-3} (Langer et al. 1995; Heithausen 2002; Sakamoto & Sunada 2003; Tachihara et al. 2012). Since they are gravitationally unbound ($M \leq 0.05 M_\odot$), they cannot be formed by gravitational instability. Although shock compression by turbulence often makes gravitationally unbound structure, it would not be easy to make very small-

scale structure (< 0.1 pc) by shock compression alone. Firstly, the shock compresses the gas as a whole, and thus cannot make fragments. Since turbulence has eddies of various spatial scales, one may imagine that the shock compression at small scale eddied can make very small-scale structures or fragments. But it should be noted that the turbulence (i.e. velocity dispersion in molecular clouds) becomes subsonic at < 0.1 pc according to Larson's law (see e.g. Heyer & Brunt 2004). Structures smaller than this scale thus cannot be formed by shock compression by turbulence. If the shocked molecular gas is thermally unstable, it could generate very small-scale fragments. The effect of thermal instability on the shocked molecular gas must be explored.

In this paper, we examine the thermal stability of shocked gas in molecular clouds using one-dimensional hydrodynamic simulations including detailed cooling, heating and chemical processes. Although our main target is molecular clouds, we also calculate one model of CNM, in order to compare our results with Koyama & Inutsuka (2000), and to compare the e-folding numbers in CNM and molecular clouds. This paper is organized as follows. In 1.2, we describe our physical and chemical models. Then, we explain the condition for the thermal instability and how we evaluate the growth of perturbation in 1.3. In 1.4, we show the results of our simulations of shock propagation in CNM and molecular clouds. Finally, we summarize our results in 1.5.

1.2 The model

We investigate the evolution of ISM swept by a shock wave in a plane-parallel gas. Figure 1.1 schematically shows the configuration of our model; we consider a collision of oppositely oriented gas flows which have the same density, temperature and chemical composition. The external radiation irradiates both ends of the numerical domain. We calculate the temporal variation of temperature, density, and chemical composition in the shocked region.

1.2.1 Basic Equations

We solve the following equations:

$$\partial_t U(t,x) + \partial_x F_x = S$$

$$
\begin{aligned}
U &= (\rho, \rho v_x, E) \\
F_x &= \begin{pmatrix} \rho v_x \\ \rho v_x^2 + p \\ (E+p) v_x \end{pmatrix} \\
S &= \begin{pmatrix} 0 \\ 0 \\ \rho\,(\Gamma - \Lambda) \end{pmatrix} \\
E &= \frac{p}{\gamma - 1} + \frac{\rho v_x^2}{2} \quad ,
\end{aligned}
$$

where ρ, v_x, p, γ, Γ and Λ are the gas mass density, velocity, thermal pressure, ratio of specific heat, heating and cooling rate per unit mass, respectively. We use an operator-splitting technique to solve these equations, which are split into three parts: (1) ideal hydrodynamics, (2) cooling and heating, and (3) chemical reactions (e.g. Inoue & Inutsuka 2008). The first part, ideal hydrodynamics, is calculated by employing a second-order Godunov method with Lagrangian coordinates (Van Leer 1979). We solve the exact Riemann problem iteratively at each grid cell interface to calculate numerical fluxes, and determine the position of grid cell interface in the next time step. Thus, we can appropriately calculate small-scale compressed dense regions and large-scale pre-shock regions at once. The energy equation

$$
\frac{\partial E}{\partial t} = \rho\,(\Gamma - \Lambda)
$$

is solved by the second-order explicit method. Temporal variation of the number density of chemical species is determined by the rate equations

$$
\frac{dn_i}{dt} = \sum_j k_{ij} n_j + \sum_{j,l} k_{ijl} n_j n_l,
$$

where k is the rate coefficient of the chemical reactions. The rate equations are calculated by a first-order implicit method (Hersant et al. 2009).

The time step of the integration is set to be small enough to satisfy the CFL condition, and to be much smaller ($\lesssim 4$ %) than the cooling time scale of the gas. The details of the physical and chemical processes considered in our model are described in the following.

1.2.2 Heating and Cooling Processes

A full list of the thermal processes included in our model is listed in Table 1.1. Our model includes the cooling by the line emission of H, C[II], O[I], and CO with the effect of

radiative trapping, recombination on grains, and dust-gas collision. We adopt the formula of escape probability by de Jong et al. (1980) for the line cooling by C[II] and O[I], and by Hollenbach & McKee (1979) for CO. The escape probability is a function of the column density of the molecule or atom $N_i = \int n_{\rm i} dx$; the number density is integrated from the edge of the numerical domain to the center of each grid cell. Since our model is 1D, we calculate the escape probabilities towards the right-hand-side and left-hand-side edges of the numerical domain, and use the average of these two values. Gas is also cooled by collisions with dust; the dust temperature is set to 10K (e.g., section 5 of Tielens 2005). Heating processes include photo-electric heating by PAH (Bakes & Tielens 1994), cosmic ray (Goldsmith & Langer 1978), and H_2 photo-dissociation (Black & Dalgarno 1977). In the calculation of photo-electric heating, we consider the attenuation of external radiation. Visual extinction, $A_{\rm V}$, is calculated by

$$A_{\rm V} = \frac{\int n_{\rm H} dx}{1.89 \times 10^{21}\ {\rm cm}^{-2}}\ \ {\rm mag}$$

where the numerator is the column density of hydrogen nuclei integrated from the edge of the numerical domain to the center of each grid cell (e.g. Mathis et al. 1983).

1.2.3 Chemical reactions

We calculate the chemical reaction network in the gas phase, which consists of 462 species and 9578 reactions. Chemical reactions and rate coefficients are adopted mainly from OSU network (http://www.physics.ohio-state.edu/~eric), which is developed for interstellar chemistry. Namely, we use the network of Garrod & Herbst (2006) at $T \leq 100$K and Harada et al. (2010) (see also Harada et al. (2012), the errata of Harada et al. (2010)) at $T > 100$K. These networks contain cosmic ray ionization, ion-molecule reactions, neutral-neutral reactions, recombination of ion, photo reactions, and grain surface reactions. We also include the collisional dissociations in Table A1 of Willacy et al. (1998), but some rate coefficients are modified (see the appendix of Furuya et al. (2012)). We do not consider grain-surface reactions except for H_2 formation. Cosmic-ray ionization rate is set to be 1.3×10^{-17} s^{-1}. In the model of CNM gas, the total column density of hydrogen nuclei is only $N_{\rm H} = 1.0 \times 10^{20}$ cm^{-2}, and the molecules are destroyed by photo reactions. We take

into account the self-shielding effects of H_2, CO and C atom referring to Lee et al. (1996) and Tielens & Hollenbach (1985); the shielding factors are given as a function of A_v and the column densities of specific species integrated from the edges of the numerical domain to each grid cell at every time step. Elemental abundances in the gas phase are listed in Table 1.2.

1.2.4 Initial and Boundary conditions

The initial temperature and chemical composition of the colliding gases are determined by calculating the thermal and chemical equilibrium. In the model of CNM, these initial conditions vary spatially depending on the visual extinction A_v at each position in the numerical domain. In the model of molecular clouds, A_v is set to be 5 mag for all grid cells; our numerical domain is an embedded small portion of the molecular cloud. In total, we calculate one CNM model and 45 molecular cloud models. The model parameters are summarized in Table 1.3.

Our initial condition of the CNM is basically the same as that of Koyama & Inutsuka (2000) (see their §3.4); we assume the number density to be $n_H = 10$ cm^{-3}. Thermal equilibrium determines the gas temperature, which is about 110 K at any position. The velocity of the colliding gas V_{fluid} (see Figure 1.1) is 10km/s, which corresponds to the velocity of gas flow associated with old supernova remnants. Total column density of hydrogen nuclei is set to be 1.0×10^{20} cm^{-2}, i.e. $A_v \simeq 0.05$ mag.

For the molecular cloud models, we explore the parameter space of the number density n_H: 1.0×10^2, 3.0×10^2, 1.0×10^3, 3.0×10^3 and 1.0×10^4 cm^{-3}. The velocity V_{fluid} ranges from 0.5 to 4.5 km s^{-1}, referring to the turbulent velocities in molecular clouds (Larson 1981; Fukui et al. 2008). We also investigate a model with $V_{fluid} = 10$ km s^{-1}, which is a typical velocity of protostellar outflows (e.g., Moriarty-Schieven & Snell 1988).

In the model of the CNM, the size of our numerical domain L_{cal} is 3.24 pc, which covers the whole region of the CNM. In order to calculate the post-shock region with a high spatial resolution, we set 225 grid cells at $x < L_{in}$, and 35 grid cells at $x > L_{in}$ (see Figure 1.1). Initially, L_{in} is 0.972 pc. Both L_{cal} and L_{in} change with time, since we are using Lagrangian coordinates. In the models of molecular clouds, our numerical domain varies

from 0.01 pc to 0.28 pc depending on the model parameters (see Table 1.3). The numerical domain is divided into 300 grid cells with equal intervals.

We adopt the free-boundary condition;

$$\frac{\partial \rho}{\partial x} = 0, \quad \frac{\partial p}{\partial x} = 0, \quad \frac{\partial v_x}{\partial x} = 0,$$

i.e. we assume that the physical values of left and right side of boundary are the same when we solve the exact Riemann problem at boundary. Basically, the boundary condition is not important, because we stop the calculation before the shock wave reaches the boundary.

1.3 Amplitude of thermal instability

Balbus (1986) showed that for any unperturbed state, the gas is thermally unstable if

$$\left[\frac{\partial}{\partial s}\left(\frac{\Lambda - \Gamma}{T}\right)\right]_A < 0, \tag{1.1}$$

where s is specific entropy, T is temperature, and A is a thermodynamic variable kept constant in the perturbation. Since the ISM is mostly in pressure equilibrium, the isobaric condition, $A = p$, is satisfied, which leads to

$$\left[\frac{\partial}{\partial T}\left(\frac{\Lambda - \Gamma}{T}\right)\right]_p < 0. \tag{1.2}$$

Schwarz et al. (1972) and Koyama & Inutsuka (2000) performed a linear analysis of thermal instability in isochorically cooling gas and isobarically contracting gas, respectively. When the gas is thermally unstable, the density perturbation grows as $\rho = \rho_0 \exp(\sigma\, t)$. The growth rate in isobarically contracting gas is

$$\begin{aligned} \sigma &= -\frac{m\, T\, (\gamma - 1)}{\gamma\, k_{\rm B}} \left[\frac{\partial}{\partial T}\left(\frac{\Lambda - \Gamma}{T}\right)\right]_p \\ &= \frac{1}{\gamma}\left\{\frac{1 + s_\rho - s_T}{\tau_{\rm cool}} - \frac{1 + r_\rho - r_T}{\tau_{\rm heat}}\right\}, \end{aligned} \tag{1.3}$$

$$s_\rho = \partial(\ln \Lambda)/\partial(\ln n), \quad s_T = \partial(\ln \Lambda)/\partial(\ln T),$$

$$r_\rho = \partial(\ln \Gamma)/\partial(\ln n), \quad r_T = \partial(\ln \Gamma)/\partial(\ln n),$$

where m is the mean molecular mass, and $\tau_{\rm cool} \equiv k_{\rm B}\, T/(\gamma - 1)/(m\, \Lambda)$ and $\tau_{\rm heat} \equiv k_{\rm B}\, T/(\gamma - 1)/(m\, \Gamma)$ are the cooling and heating time scales, respectively. σ is a function of density

and temperature, that changes with time as the gas goes through the shock wave and enters the cooling region. When the gas is thermally unstable, σ takes a positive value.

In this paper, we evaluate the integrated e-folding number $\int \sigma dt$ as an indicator of the amplification of the perturbation, where the e-folding number is calculated for each fluid element in Lagrangian coordinate, and the integral is executed only when the Balbus criterion (Eq 1.1) is satisfied. Then, using the e-folding number, we obtain the amplification of the thermal instability $\exp(\int \sigma dt)$.

In the linear analysis, the growth rate is a function of the wavelength of the perturbation, and Eq. (1.3) is the rate for the most unstable mode at

$$\lambda_{\rm max} = \sqrt{l_{\rm F} l_{\rm a}}. \tag{1.4}$$

The Field length $l_{\rm F}$ is

$$l_{\rm F} = \left\{ \frac{\kappa T}{\rho \left(\Gamma - \Lambda\right)} \right\}^{1/2}, \tag{1.5}$$

where the thermal conductivity κ is $2.5 \times 10^3 T^{0.5}$ cm^{-1} K^{-1} s^{-1} (Parker 1953). The acoustic length $l_{\rm a}$ is

$$l_{\rm a} = c_{\rm s} \left(\frac{e}{\Gamma - \Lambda} \right), \tag{1.6}$$

where $c_{\rm s}$ is the sound speed, e is the specific internal energy, and $e/(\Gamma - \Lambda)$ is the net cooling time scale (Field 1965). It should be noted, however, that the dependence of the growth rate on perturbation wavelength is considerably weak around the most unstable wavelength. The growth rate is comparable to equation (1.3) in the wavelength range of

$$l_{\rm F} < \lambda < l_{\rm a} \tag{1.7}$$

(Field 1965, see also Appendix B of Koyama & Inutsuka 2000).

Ideally, the growth of density perturbation should be measured in hydrodynamic simulations starting from an initial condition with small amplitude perturbations. But it is not easy in practice. First of all, the thickness of the unstable layer is comparable to or smaller than the most unstable wavelength (see Figure 1.3). In one dimensional flow, the perturbation grows as long as Eq. (1.1) is satisfied, but when the gas is compressed to be in thermally stable state, the perturbation is dispersed, which is an artifact. In 2D and/or 3D simulations, large scale perturbations up to the acoustic length $l_{\rm a}$ can grow in

directions *parallel* to the shock front, and these clump structures remain in the post-shock regions (e.g. Inoue & Inutsuka 2008). The 2D/3D simulation is, however, very time consuming, especially if we are to resolve the perturbations with very small wavelengths. It is well established that the growth rate derived from the linear analysis is applicable to non-linear regime of thermal instability. For instance, we can see in Figure 1 of Inoue et al. (2007) that the isobaric condition, which is required for the thermal instability to grow with the linear growth rate, is met throughout the evolution without interceptive feedback effects. Therefore, it is reasonable to estimate the amplification of the density perturbation by integrating the e-folding number along the 1D flow. It should at least be done before investing a large computational time on 2D hydrodynamic simulation with perturbation and very high spatial resolution. We also note here that our present work is analogous to Koyama & Inutsuka (2000); they performed 1D shock calculation to find that the gas becomes thermally unstable in the shock-compressed layer and predicted that small clumps would be formed. Later, Koyama & Inutsuka (2002) indeed showed that such clumps are formed in the 2D simulation.

1.4 Results

We have calculated the generation and propagation of shock waves in CNM and molecular clouds by solving the basic equations in §2.1. In the following, we show the spatial distribution of physical parameters and the e-folding number when the shock wave reaches a steady state.

1.4.1 Shock Propagation in CNM

Figure 1.2 (a) shows the distribution of temperature, number density of hydrogen nuclei ($n_{\rm H}$), thermal pressure, and integrated e-folding number at $t = 88000$ yr in the CNM model. A similar simulation was performed by Koyama & Inutsuka (2000). Temperature and density distributions in Figure 2 are indeed similar to Figure 7 of Koyama & Inutsuka (2000), who found that the shocked CNM evolves through a thermally unstable state. The gray shade in Figure 1.2 depicts the thermally unstable region, in which the condition (1.1) is satisfied. CNM becomes thermally unstable immediately behind the shock and

then evolves to a thermally stable dense gas with basically isobaric condition (see Figure 7 (a) of Koyama & Inutsuka 2000). The main coolants are CII(158μm) and OI(63μm). Now, we go one step further from Koyama & Inutsuka (2000) and calculate the e-folding number. The integrated e-folding number $\int \sigma dt$ is approximately 5, which means that the density fluctuation grows by a factor of $\exp(5) \simeq 150$. Note that the density profile shown in Figure 1.2 is the unperturbed value. For example, if the pre-shock gas has a density fluctuation of 10%, i.e. 11 cm^{-3} in the pre-shock gas of 10 cm^{-3}, the fluctuation grows by a factor of 150, 1.6×10^4 cm^{-3} in the post-shock gas of 1.0×10^3 cm^{-3}.

We also show the distribution of assorted chemical species (Figure 1.2 b). Molecular hydrogen in the pre-shock region in our model is more abundant than that of Koyama & Inutsuka (2000) due to the difference in the self-shielding model; Koyama & Inutsuka (2000) used the formulation by Tielens & Hollenbach (1985), while we use the Table 10 in Lee et al. (1996). In the dense stable region ($x \lesssim 10^{-3}$ pc), on the other hand, the H_2 abundance in our model is almost the same as that in Koyama & Inutsuka (2000). H_2 is formed by the association of H atoms on grain surfaces and destroyed by photo-dissociation. Figure 1.2 (b) also shows the abundances of C^+, C and CO. Although Koyama & Inutsuka (2000) did not show the spatial distribution of CO, they reported that 0.02 % of the carbon is in CO in the dense stable gas in the post-shock region. In our model 0.03 % of carbon is in CO. It should be noted that we solve the detailed chemical network, whereas Koyama & Inutsuka (2000) adopted a simplified chemical model that assumed a direct conversion of C^+ to CO without accounting explicitly for the intermediate reactions. Consistency of our model results with Koyama & Inutsuka (2000) validates their simplified model.

Figure 1.2 (c) shows the Field length, acoustic length and the most unstable wavelength of perturbation $\sqrt{l_{\rm F} l_{\rm a}}$ in the unstable region. The Field length is $10^{-5} - 10^{-3}$ pc and the acoustic length is $10^{-3} - 10^{-1}$ pc. The most unstable wavelength ranges from 10^{-4} to 10^{-2} pc, which coincides with the size of the tiny scale structures observed in CNM, $\sim 10^{-3}$ pc (see Table 1 of Heiles 1997). Such tiny structures can be formed by thermal instability (Koyama & Inutsuka 2000).

1.4.2 Shock Propagation in Molecular Clouds

Figure 1.3 (a) shows the spatial distribution of temperature, number density of hydrogen nuclei ($n_{\rm H}$), thermal pressure, and integrated e-folding number $\int \sigma dt$ in the model with 4.5 km s^{-1} and a pre-shock density $n_{\rm H} = 100$ cm^{-3} at $t = 53000$ yr. The gas becomes thermally unstable immediately behind the shock, where the gas temperature reaches near 1000 K. The gas evolves in the post-shock region with the isobaric condition. The main coolant is CO in this warm gas. The integrated e-folding number is 1.25; if we calculate the HD simulation with a small perturbation, it grows only by a factor of 3.5.

Figure 1.3 (b), on the other hand, shows a model with a higher initial density $n_{\rm H} = 1 \times 10^4$ cm^{-3} at $t = 1500$ yr. In this model, the post-shock gas becomes thermally unstable right behind the shock front, but then becomes stable, although the temperature (several hundreds of K) in this region is similar to that in the unstable post-shock gas in Figure 1.3 (a). Once the number density $n_{\rm H}$ reaches several times 10^5 cm^{-3}, the dust-gas collisional cooling becomes dominant and the gas becomes thermally unstable again. The integrated e-folding number is even smaller than in the model of Figure 1.3 (a).

Figure 1.3 (c) and (d) show the spatial distribution of the Field length, acoustic length and the most unstable wavelength $\sqrt{l_{\rm F} l_{\rm a}}$ in the two models of molecular gas. In the model with higher gas density, the cooling rate is higher (see below), and thus these scale lengths become shorter (see Eq (1.5) and (1.6)).

We summarize the integrated e-folding number in our molecular cloud models in Table 1.4. We can see that the shocked molecular gas is unstable when $V_{\rm fluid}$ is larger than $\sim 1.5 \log(n_{\rm H}\,[{\rm cm}^{-3}]) - 2$ km s^{-1}, and that the integrated e-folding number increases with increasing $V_{\rm fluid}$ and decreasing initial gas density. These dependences can be understood as follows. When the net cooling rate per unit mass L is proportional to $n^\beta T^\gamma$, the criterion for thermal instability by Balbus (1986) can be rewritten as $\beta - \gamma + 1 > 0$ (see Appendix A.1). The gas is more unstable when β is larger and γ is smaller. In other words, the perturbation grows faster when the dependence of the cooling rate on the temperature is weaker and/or dependence of the cooling rate on gas density is stronger. The cooling rate actually is a more complicated function of density and temperature than a power law

$n^\beta T^\gamma$. But we can define β and γ as a local tangent in logarithmic plot. Figures 1.4 (a) and (b) show the local tangent, β and γ, of the cooling rate by CO rotational lines as a function of temperature and density at a typical molecular cloud condition. We can see that β is larger at lower densities and γ is larger at low temperatures. In general, when the gas temperature is high enough to excite the coolant species (e.g., C^+, CO), the cooling rate does not significantly decrease as the temperature is lowered. When the gas temperature is comparable to the upper state energy of the line, on the other hand, the cooling rate decreases steeply as the gas temperature is lowered. The dependence of β on density can be understood by considering the critical density, which is $3.3\times10^6(T/1000)^{0.75}$ cm^{-3} for CO rotational lines (McKee et al. 1982). When the gas density is much smaller than the critical density, the cooling rate per unit volume is proportional to n^2, whereas at the critical density or higher, the dependence is weaker than n^2 because of collisional de-excitation (see e.g., section 2.3.1 of Tielens 2005).

In Table 1.4, asterisks indicate that the dust-gas collisional cooling dominates over the CO cooling in the model. The cooling rate by dust-gas collision per unit mass is given as

$$1.2\times10^{31}n_{\rm H}\,(T_{\rm gas}/1000)^{0.5}\,(100\text{Å}/a_{\rm min})\times[1-0.8\exp(-75/T_{\rm gas})]\,(T_{\rm gas}-T_{\rm dust})/m\ \ \mathrm{erg\ g^{-1}\ s^{-1}},$$

where m is the mean molecular mass and we set $a_{\rm min}=100$ Å and $T_{\rm dust}=10$ K (Hollenbach & McKee 1989). It is obvious that β is always 1 in any density region, and that dust-gas collisional cooling is important at high densities. Figure 1.4 (c) shows the power index γ. The cooling rate is proportional to $T_{\rm gas}^{1.5}$ when $T_{\rm gas}>>T_{\rm dust}$, but γ becomes larger than 1.5 when $T_{\rm gas}\simeq T_{\rm dust}$ (see Appendix A.2). Since the dust temperature is 10 K in our model, the gas is more unstable at higher temperatures.

1.5 Summary and Discussion

We performed the one-dimensional hydrodynamic simulations with the effects of heating, cooling and chemical reactions in order to study the thermal stability of shocked gas in CNM and molecular clouds. Taking advantage of the fact that the growth rate derived from the linear analysis (Schwarz et al. 1972; Koyama & Inutsuka 2000) is applicable to the non-linear regime in thermal instability, we calculate the e-folding number along the flow

to evaluate the amplification of density perturbation behind the shock wave. Our findings are as follows

- Both CNM and molecular cloud can be thermally unstable behind a shock wave.
- A molecular cloud becomes thermally unstable behind a shock when $V_{\rm fluid} \gtrsim 1.5\ \log(n\,[{\rm cm}^{-3}]) - 2\ {\rm km\ s}^{-1}$.
- The integrated e-folding number in the shocked molecular cloud increases with increasing $V_{\rm fluid}$ and decreasing pre-shock density.
- The wavelength, $l_{\rm F} \lesssim \lambda \lesssim l_{\rm a}$, the perturbation of which can grow within the cooling time scale, ranges from 10^{-5} pc to 0.1 pc in the CNM, and from 10^{-7} pc to 0.1 in molecular clouds. The unstable wavelength is a decreasing function of pre-shock density and fluid velocity, since both the Field length $l_{\rm F}$ and acoustic length scale $l_{\rm a}$ decrease with gas density.

The unstable wavelength of the thermal instability coincides with the size of the tiny scale structures observed in the CNM (Heiles 1997; Stanimirović & Heiles 2005) and molecular clouds (Langer et al. 1995; Heithausen 2002; Sakamoto & Sunada 2003; Tachihara et al. 2012). Thermal instability could thus explain the formation of such small gravitationally-unbound clumps in the ISM. In the CNM, the initial perturbation is amplified by a factor of 10^2 in the thermally unstable region behind a shock. In molecular clouds, on the other hand, the initial perturbation is amplified only by a factor of a few. It should be noted, however, that the super-sonic velocity dispersion is ubiquitous in molecular clouds. Small clumps would be formed if the molecular cloud is swept by multiple shocks.

Finally, we discuss the fate of the structure formed by the thermal instability. In the HI medium, the CNM can coexist with the WNM thanks to the thermally bistable nature (Field et al. 1969). If the molecular clouds are isothermal uni-phase medium, the density fluctuations enhanced by the thermal instability could exist only in the very narrow shock transition layer, because the post-shock gas eventually returns to the same temperature as the pre-shock gas. However, recent numerical simulations of molecular cloud formation (e.g., Banerjee et al. 2009; Inoue & Inutsuka 2012) have shown that molecular clouds are

composed of the cold molecular gas ($T \sim 10$ K and $n > 100$ cm^{-3}) and the *non-equilibrium* diffuse warm gas ($T > 1000$ K and $n \sim 1$ cm^{-3}). The diffuse warm component, which is generated by the cloud-forming shocks at the envelope of molecular cloud, is in high pressure and thermally unstable. The implication of this result is twofold. Firstly, it shows that a bistability of thermal equilibrium gas is not needed for density fluctuations to survive in post shock gas. Secondly, in such a "non-equilibrium two-phase medium", the structure formed by the thermal instability behind the shock within molecular clouds would be more likely to survive in the non-equilibrium diffuse gas. If the perturbed gas can fragment and coexist with the diffuse gas, the very small-scale structure could survive until at least the diffuse gas cools down ($\sim 0.1 - 1$ Myr). But it is still an open question, and multi-dimensional simulations are necessary to confirm our expectation.

Cooling & heating process	reference
Ly-α cooling	Spitzer (1978)
C^+ fine structure cooling(158μm)	de Jong et al. (1980), Hollenbach & McKee (1989)
O fine structure cooling(63μm)	de Jong et al. (1980), Wolfire et al. (2003)
CO rotational cooling	Hollenbach & McKee (1979), Hosokawa & Inutsuka (2006)
CO vibrational cooling	Hollenbach & McKee (1989)
Cooling due to recombination on grains	Bakes & Tielens (1994)
Cooling by the collision with dust	Hollenbach & McKee (1989)
Photoelectric heating by PAH	Bakes & Tielens (1994), Wolfire et al. (2003)
Cosmic ray heating	Goldsmith & Langer (1978)
H_2 photo-dissociation heating	Black & Dalgarno (1977)

Table 1.1: Heating and cooling processes

element	abundance	element	abundance
He	9.75×10^{-2}	Fe	2.47×10^{-9}
O	4.5×10^{-4}	Na	2.25×10^{-9}
C	3.02×10^{-4}	Mg	1.09×10^{-8}
N	2.47×10^{-5}	P	2.16×10^{-10}
S	9.14×10^{-8}	Cl	1.0×10^{-9}
Si	2.47×10^{-9}		

Table 1.2: Elemental abundance in the gas phase relative to hydrogen

$n_{\rm H}$ [cm^{-3}]	T [K]	G_0 [1]	H atom [2]	H_2 [2]	C atom [2]	CO [2]	C^+ [2]	$L_{\rm cal}$ [3] [pc]
CNM								
10	110	1.7	1.0	2.5(-5)	3.8(-8)	1.8(-12)	3.0(-4)	3.24
molecular cloud								
100	22	1.0	1.0(-2)	0.49	1.2(-4)	1.64(-4)	1.5(-5)	0.28
300	15	1.0	3.0(-3)	0.5	1.6(-6)	3.0(-4)	3.3(-7)	0.15
1×10^3	13	1.0	1.0(-3)	0.5	3.8(-7)	3.0(-4)	1.1(-7)	0.05
3×10^3	10.5	1.0	4.2(-4)	0.5	9.7(-8)	3.0(-4)	4.3(-8)	0.02
1×10^4	9.3	1.0	1.3(-4)	0.5	2.3(-8)	3.0(-4)	1.4(-8)	0.01

Table 1.3: Initial state

[1]External FUV radiation normalized to the local interstellar radiation field (1.6×10^{-3} ergs cm^{-2} s^{-1}) of Habing (1968).
[2]Relative abundance of chemical species to hydrogen nuclei($n_{\rm H}$). $a(-b)$ means $a\times10^{-b}$.
[3]Initial numerical domain (see Figure 1.1).

V_{fluid} [km s^{-1}]	n_H [cm^{-3}] 10^2	3×10^2	10^3	3×10^3	10^4
0.5	×	×	×	×	×
1.0	0.08	×	×	×	×
1.5	0.35	0.005	×	×	×
2.0	0.6	0.1	×	×	×
2.5	0.7	0.25	0.03	×	×
3.0	0.9	0.35	0.1	0.002	×
3.5	1.0	0.5	0.2	0.04	×
4.0	1.1	0.6	0.3	0.1	0.02
4.5	1.25	0.7	0.4	0.2*	0.3*
10.0	2.0	1.4	1.3*	1.3*	1.3*

Table 1.4: Integrated e-folding number in the shocked molecular cloud. The cross mark indicates that the gas is fully stable. The asterisk indicates that the dust-gas collisional cooling is the dominant cooling in the model.

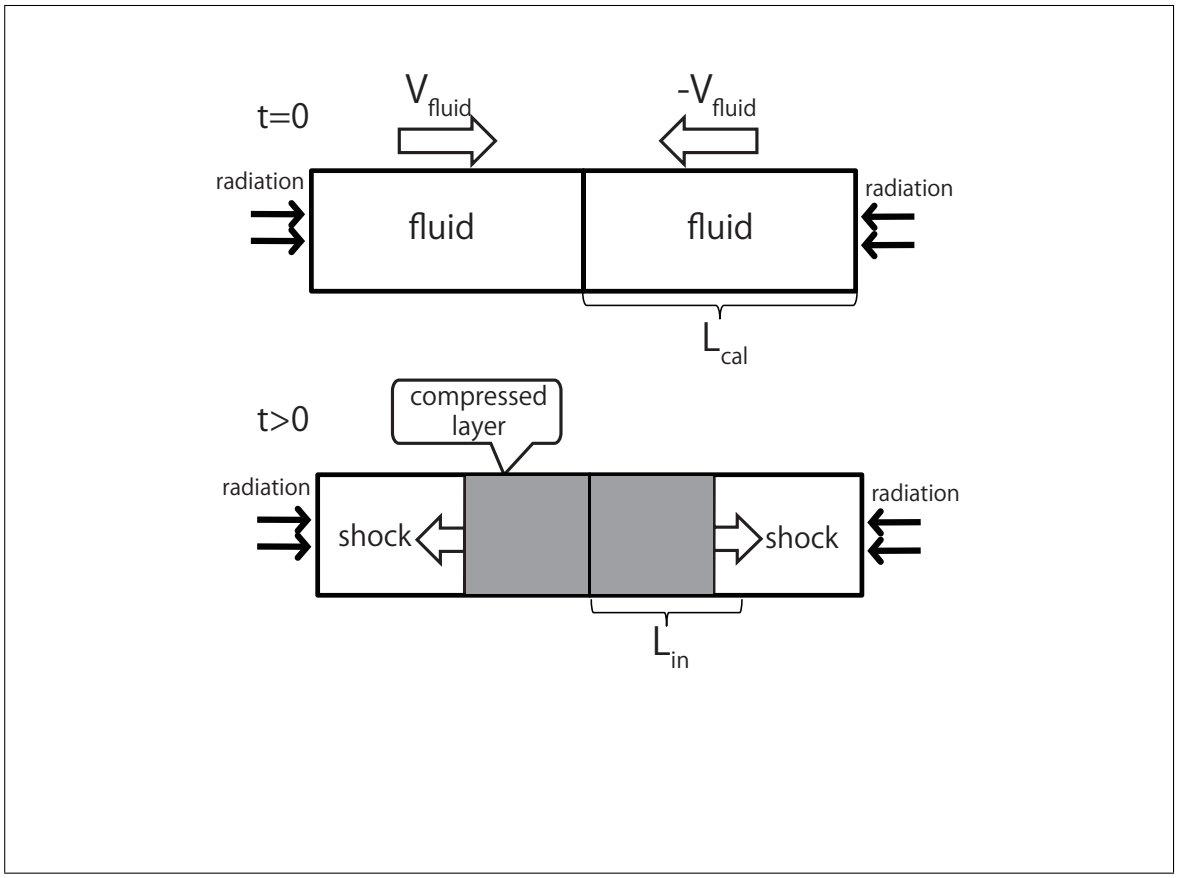

Figure 1.1: Schematic view of our 1D shock model

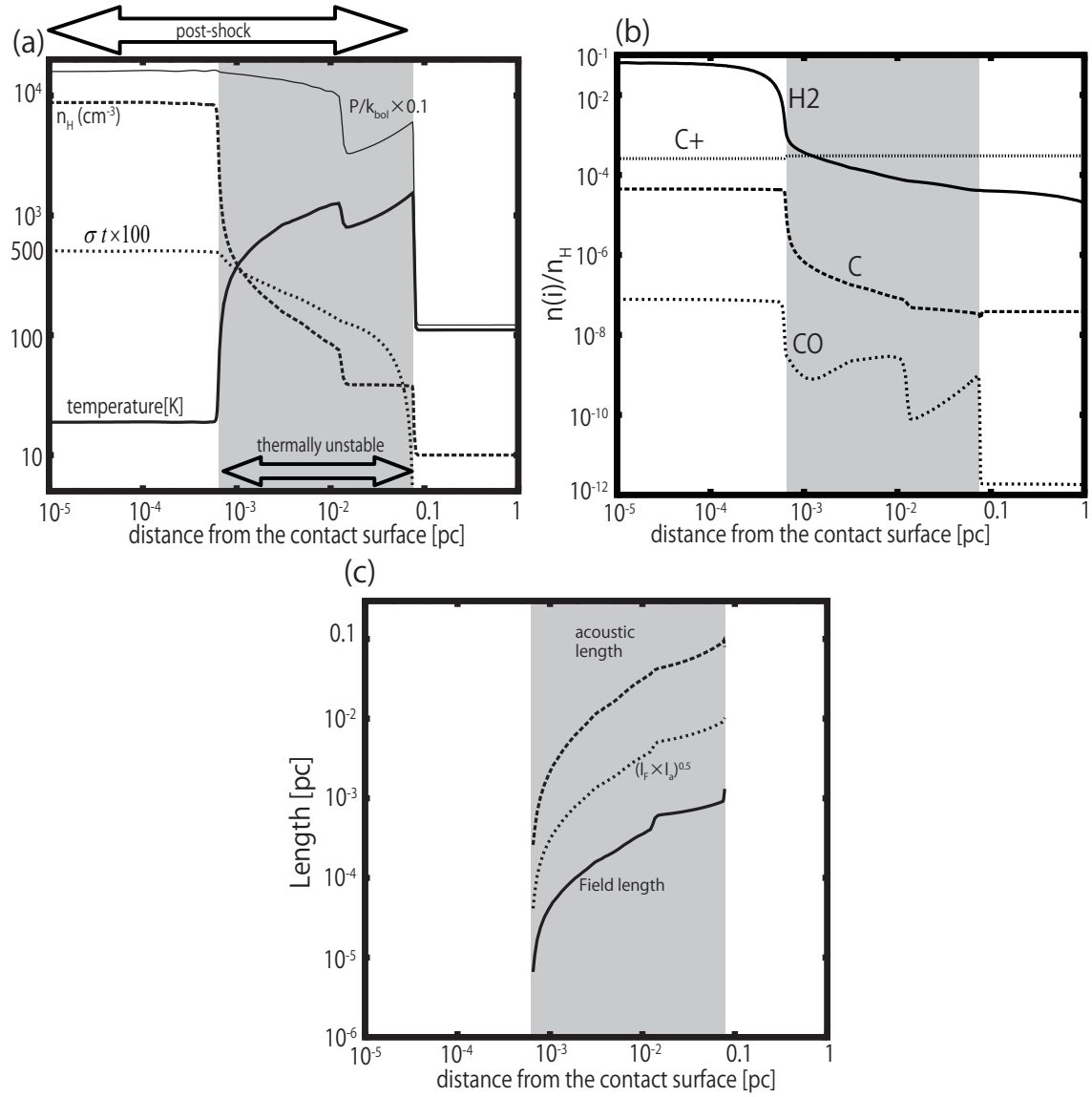

Figure 1.2: (a) Spatial distribution of temperature (*solid line*), number density of hydrogen nuclei (*dashed line*), thermal pressure (*thin-solid line*), and integrated e-folding number σt (*dotted line*) at $t = 88000$ yr. Thermally unstable region is shaded in gray. (b) Spatial distribution of H_2, C, CO and C^+ abundances with respect to hydrogen nuclei at $t = 88000$ yr. (c) Spatial distribution of Field length, acoustic length and most unstable wavelength $\sqrt{l_F l_a}$.

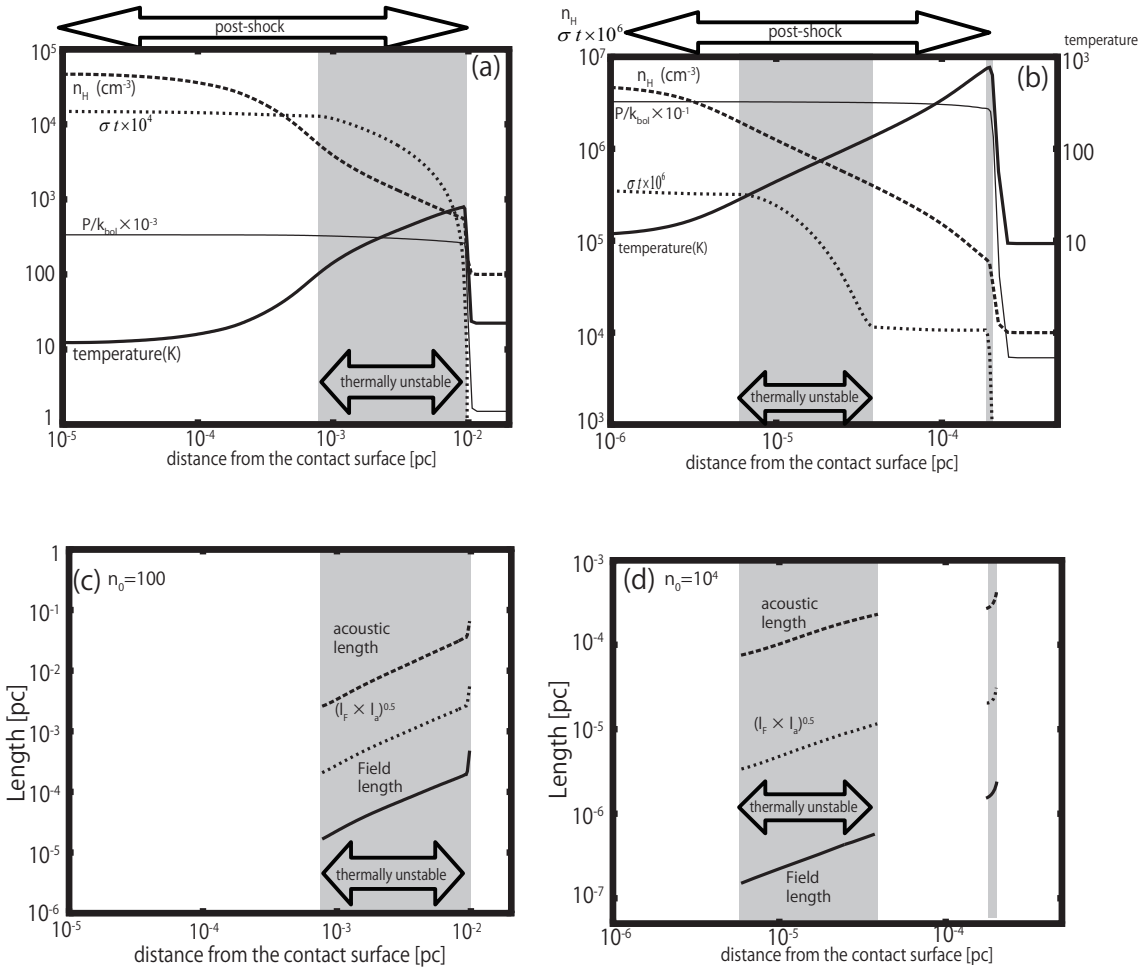

Figure 1.3: Spatial distribution of temperature (*solid line*), number density of hydrogen nuclei (*dashed line*), thermal pressure (*thin-solid line*), and integrated e-folding number (*dotted line*) in the model with $n_{\rm H} = 10^2$ cm^{-3} at $t = 53000$ yr (a), and in the model with $n_{\rm H} = 10^4$ cm^{-3} at $t = 1500$ yr (b). (c), (d) Spatial distribution of Field length, acoustic length and the most unstable wavelength $\sqrt{l_{\rm F} l_{\rm a}}$ in the models with high and low initial densities. The thermally unstable region is shaded in gray, as in Figure 2.

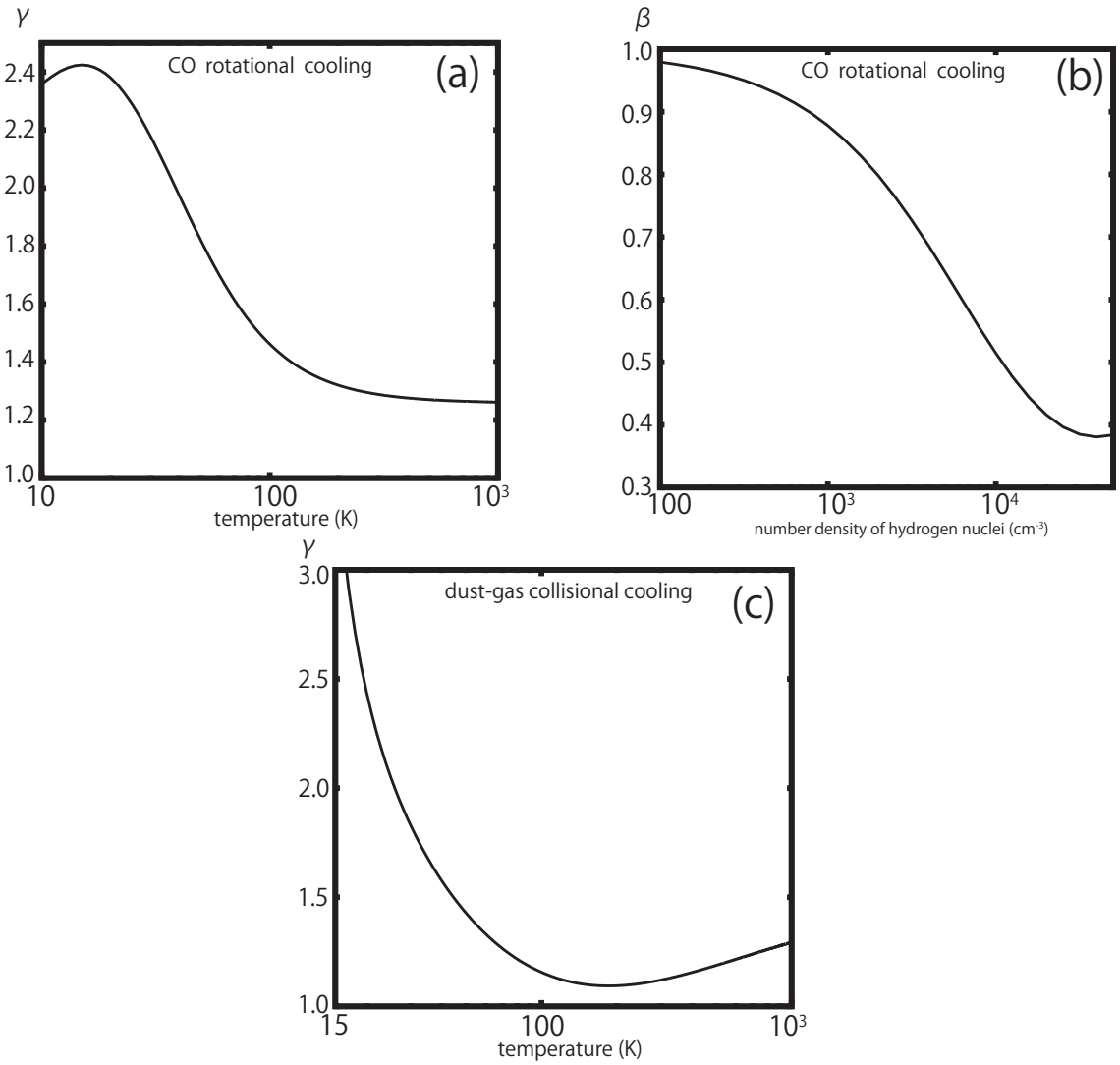

Figure 1.4: (a)-(b) The power-law index of temperature, $\gamma = \partial \ln(\Lambda)/\partial \ln(T)$, is calculated at a given density $n_{\rm H} = 10^3$ cm^{-3}, CO abundance of 1.6×10^{-4} and CO column density of $N_{\rm CO} = 7.0 \times 10^{17}$. The power-law index of density, $\beta = \partial \ln(\Lambda)/\partial \ln(n)$, is calculated at $T = 100$ K, CO abundance of 1.6×10^{-4} and $N_{\rm CO} = 7.0 \times 10^{17}$. (c) The power-law index γ of the dust-gas collisional cooling is calculated at $T_{\rm dust} = 10$ K.

Chapter 2

Phosphorous chemistry in the shocked region L1157 B1 [1]

2.1 Introduction

Although the solar abundance of phosphorus is 3×10^{-7} with respect to H (Asplund et al. 2009), only a small number phosphor-containing molecules have been observed in space. PN is the only P-bearing species detected in *warm* molecular clouds (e.g., Turner & Bally 1987; Turner et al. 1990), whereas other species (CP, PO, HCP, CCP, PH_3) have been detected in the envelopes of evolved stars (e.g., IRC+10216) (Guélin et al. 1990; Tenenbaum et al. 2007; Agúndez et al. 2007; Halfen et al. 2008; Agúndez et al. 2008). Turner & Bally (1987) detected PN in Ori(KL), W51M, and Sgr B2, whereas Matthews et al. (1987) did not detect PO in Ori(KL) or Sgr B2. Considering the non-detection of PO, Turner & Bally (1987) suggested that PN is formed by grain disruption. On the other hand, Millar et al. (1987) calculated the P-chemistry considering related reactions (e.g., PO + N $\rightarrow$ PN + O), and showed that the observed PN abundance and non-detection (i.e., the upper limit) of PO can be reproduced by gas-phase chemistry at low temperature (50 K). Later, Charnley & Millar (1994) showed that PN becomes abundant within 10^4 yr in hot core models; assuming that P is initially in the form of PH_3 ice, they calculated the gas-phase chemistry after the evaporation of PH_3.

Recently, Yamaguchi et al. (2011) detected PN in a low-mass star-forming region, L1157 B1, for the first time. L1157 is a dark cloud harboring a Class 0 low-mass protostar,

which drives a well-collimated molecular outflow with the dynamical age of 1.8×10^4 yr (Umemoto et al. 1992). L1157 B1 is a shocked region formed by interactions between the blue-shifted molecular outflow and ambient gases. Since B1 is distant from the protostar, the "pure" shock chemistry can be investigated. Many observational studies of the B1 region have been conducted to investigate physical and chemical conditions (e.g., Bachiller & Pérez Gutiérrez 1997; Hirano & Taniguchi 2001; Sugimura et al. 2011). The kinetic temperature is estimated to be $50-170$ K (Hirano & Taniguchi 2001), and H_2 density is in the range of 10^4 cm^{-3} (Hirano & Taniguchi 2001) to 10^5 cm^{-3} (Bachiller & Pérez Gutiérrez 1997) in the shocked region. Previous work concluded that C-shock occurs at B1 (Gusdorf et al. 2008; Viti et al. 2011). PN is detected also towards the shocked region L1157 B2. The abundance relative to H_2 is estimated to be $n(\mathrm{PN})/n(\mathrm{H_2}) \simeq (2-6) \times 10^{-10}$ towards B1 and $(3-7) \times 10^{-10}$ towards B2 (Yamaguchi et al. 2011). The PN line is blue-shifted, and the line width is as broad as 3.8 km s^{-1}. In addition, PN emission is *not* detected toward the protostar position. Yamaguchi et al. 2011 thus concluded that PN is formed by shock. A subsequent work (Yamaguchi et al., in prep) reported that PO is *not* detected at B1; the upper limit of PO abundance relative to H_2 is 2.5×10^{-10}. Detailed modeling of phosphorous chemistry in shocks and comparison of the results with these observations will improve our understanding of P chemistry.

In this work, we study the evolution of the P-bearing species in interstellar shocks. We solve the chemical reaction network along one-dimensional (1D) C-shock models, which mimic the L1157 B1 region. In 2.2, we describe the physical and chemical model. Results of the numerical calculation are presented in 2.3. In 2.4, we discuss the difference between our model and that of Charnley & Millar (1994). The dependences of P-chemistry on shock parameters are also investigated in 2.5. We summarize our conclusion in §5.

2.2 Model

We adopt the steady-state 1D C-shock model by Jiménez-Serra et al. (2008), in which temporal variations of density and temperature (neutral and ion) are given for several pre-shock densities and velocities. We make a fitting function of electron temperature, which is not included in the model of Jiménez-Serra et al. (2008), based on Draine et al. (1983) and

Flower et al. (1996). Referring to the observation of L1157 B1 (Bachiller & Pérez Gutiérrez 1997), we assume the pre-shock density $n(\mathrm{H_2}) = 1.0 \times 10^4$ cm^{-3} and velocity $v = 20$ km s^{-1}. Figure 2.1 shows the temporal variation of neutral, ion, and electron temperatures, $\mathrm{H_2}$ density, and neutral and ion velocities. We define $t = 0$ as the time when the density and temperature start to rise due to the shock. The gas is heated to $T \sim 1000$ K in 10^3 yr, but then cooled to 10 K in 10^4 yr. The gas temperature estimated from the observation, 50-170K (Hirano & Taniguchi 2001), is much lower than the peak temperature of the shock model because of the beam dilution; the beam size of Hirano & Taniguchi (2001) is ~ 0.03 pc, whereas the width of the layer heated to $T > 100$K is ~ 0.018 pc in the model.

Along the flow, we calculate the chemical reaction network, which consists of 658 species and 11285 reactions. Chemical reactions and rate coefficients are adopted mainly from the OSU network (http://www.physics.ohio-state.edu/~eric); we use the network of Garrod & Herbst (2006) at $T \lesssim 100$K and Harada et al. (2010) at $T > 100$K. We also include collisional dissociations in Table A1 of Willacy et al. (1998), as well as the reactions of $\mathrm{PH_3}$ and $\mathrm{PH_4^+}$ in Table 1 of Charnley & Millar (1994). Grain surface reactions are included in our chemical network to set up the initial abundances of pre-shock matter (see Model B described below). In the shock chemistry, however, we neglect the grain-surface reactions, because they are not effective in the shocked region within the dynamical time scale of L1157 (1.8×10^4 yr).

In C-shock, the neutral and ion temperatures are different. To evaluate the reaction rate coefficient in such flows, Flower et al. (1985) introduced effective temperature, $T_{\rm eff}$, including the streaming effect:

$$\frac{3}{2}k_{\rm bol}T_{\rm eff} = \frac{3}{2}k_{\rm bol}T_{\rm r} + \frac{1}{2}m_{\rm in}(u_{\rm i} - u_{\rm n})^2$$
$$T_{\rm r} = \frac{m_{\rm i}T_{\rm n} + m_{\rm n}T_{\rm i}}{n_{\rm i} + m_{\rm n}}$$
$$m_{\rm in} = \frac{m_{\rm n}m_{\rm i}}{m_{\rm n} + m_{\rm i}} \quad ,$$

where $u_{\rm n}$ and $u_{\rm i}$ are neutral and ion velocities, and $m_{\rm n}$ and $m_{\rm i}$ are neutral and ion masses, respectively. We also use the following formula for rate coefficients of collisional dissociation of molecules by ions

$$k = \sigma \times |u_{\rm i} - u_{\rm n}|$$

$$\sigma = 1.0 \times 10^{-16}(1 - \frac{E_0}{E_{\rm T}}) \quad {\rm cm}^2 \quad ,$$

if the kinetic energy of the relative motion of the reactants, $E_{\rm T}$ ($= \frac{1}{2} m_{\rm in} |u_{\rm i} - u_{\rm n}|^2$), is larger than the threshold energy E_0.

In this work, we consider two models. In model A, we assume that heavy-element species are completely accreted onto grain surfaces in the pre-shock gas. In model B, we calculate molecular evolution in a molecular cloud condition to set the initial abundance of the pre-shock gas.

In hot core models (e.g., Charnley & Millar 1994), it is assumed that heavy elements are completely depleted onto grain surfaces initially due to low temperature (10K) and high density ($n({\rm H_2}) \sim 10^6 - 10^7$ cm^{-3}) in prestellar cores. Chemical calculation starts when the protostar heats the core and the grain surface species are sublimated. Referring to the hot core models, we assumed that heavy elements (heavier than He) are completely depleted on grain surfaces in the pre-shock gas in Model A. We adopt the initial molecular abundances (Table 2.1) of the hot core model of Nomura & Millar (2004). They determined these initial abundances to be consistent with the observations of interstellar ices in molecular clouds and gas-phase species in hot cores. Previous studies (e.g., Draine et al. 1983; Caselli et al. 1997) showed that the sputtering of grain-surface species is effective in C-shock with 20 km s^{-1}. Jiménez-Serra et al. (2008) calculated the sputtering of dust surface species and showed that the time scale of sputtering is about 100 yr, if the initial H_2 density is 10^4 cm^{-3}. Since this sputtering time scale is much shorter than the heating time scale of neutral gas and electrons (Figure 2.1) and the chemical time scale (see §3), we simply start our calculation with all the molecules desorbed to the gas phase at t =0.

In model B, we set the initial molecular abundances by calculating the chemical evolution in a molecular cloud condition ($n({\rm H_2})$=10^4 cm^{-3}, T = 10 K), which is the same as the parameters in our pre-shock gas. Elemental abundance is the same as Model A. The molecular cloud calculation starts with atoms and ions except for hydrogen and phosphorus; H is in molecular form (Table 2.2) and P is in the solid phase (see below). We adopt the molecular abundances at $t = 1 \times 10^5$ yr as the initial condition of the shock chemistry. At the start of the shock chemistry, all ice-mantle species formed in the molecular cloud

are desorbed to the gas phase.

The initial form and abundance of phosphorous relative to hydrogen require some explanation. Although the solar abundance of phosphorous is 3×10^{-7}, P-bearing species are not detected in quiescent molecular clouds (e.g., Turner et al. 1990). If all P is in the gas phase (i.e., P^+) initially, theoretical models predict that PN abundance becomes high enough to be easily detected in molecular clouds. A significant amount of phosphorous thus should be depleted in the solid phase in quiescent clouds (e.g., Millar et al. 1987), but the dominant form of P in solid is unknown. Charnley & Millar (1994) assumed that PH_3 ice is as abundant as 1.2×10^{-8} in the prestellar core, and that only this amount of phosphorous is desorbed to the gas phase upon heating via star formation. Following Charnley & Millar (1994), we assume PH_3 abundance of 1.2×10^{-8} in Model A.

In Model B, we assume that all P is in the solid phase in molecular clouds. We then assume that a fraction of P is desorbed to the gas phase in atomic form via sputtering in the shock. To make the comparison with Model A easy, the desorbed abundance of P atoms is set to 1.2×10^{-8}. We note that the abundances of P-bearing species are proportional to the assumed elemental abundance of P (P atom or PH_3 initially) in the shocked gas. Although we assume a gaseous P abundance of 1.2×10^{-8} in our fiducial model, we vary this abundance in order to reproduce the observed abundance of PN and the non detection of PO. The result tells us how large of a fraction of P is in the relatively volatile component in the solids that is desorbed to the gas phase via sputtering in the C shock.

2.3 Result

2.3.1 Model A

Figure 2.2 shows the time evolution of P-bearing species in Model A. Abundances are relative to the number density of hydrogen nuclei ($n_{\rm H}$). Major chemical reactions of P-bearing species are shown in Figure 2.3. At first, P is in PH_3, which reacts with H atoms, converting them to P atoms:

$$\mathrm{H} + \mathrm{PH_3} \rightarrow \mathrm{PH_2} + \mathrm{H_2} \tag{2.1}$$

$$\mathrm{H} + \mathrm{PH_2} \rightarrow \mathrm{PH} + \mathrm{H_2} \tag{2.2}$$

$$H + PH \rightarrow P + H_2. \tag{2.3}$$

These reactions have activation barriers of 735K, 318K, and 416K, respectively, and thus become active only when the gas temperature is higher than ~ 100 K, i.e., from t =several 10^2 yr to a few 10^3 yr in our model. P atoms react slowly with H_3O^+ to form PO

$$P + H_3O^+ \rightarrow HPO^+ + H_2 \tag{2.4}$$

$$HPO^+ + H_2O \rightarrow PO + H_3O^+. \tag{2.5}$$

PN is then formed by the following reactions

$$PO + N \rightarrow PN + O \tag{2.6}$$

$$PH + N \rightarrow PN + H. \tag{2.7}$$

For comparison with the observation, we refer to the abundances at the dynamical time scale of the outflow of L1157, $\sim 10^4$ yr (Umemoto et al. 1992). In Figure 2.2, PN abundance is lower, and PO abundance is much higher than observed in L1157 B1. Considering the reactions (2.6) and (2.7), it is clear that the abundances of PN and PO depend on that of N atoms. In the current model, the dominant form of nitrogen is N_2, and N atoms are formed by the collisional dissociation of N_2

$$N_2 + Fe^+ \rightarrow N + N + Fe^+$$

and the following reactions

$$He^+ + N_2 \rightarrow N^+ + N + He$$

$$N_2 + \text{cosmic ray} \rightarrow N + N.$$

Collisional dissociation is effective only at $t \sim 200$ yr. The latter two reactions proceed slowly and thus produce insufficient amounts of N atoms to form PN. We note here that the initial zero abundance of N atoms would be artificial. According to theoretical models and observations (Aikawa et al. 2001; Maret et al. 2006), nitrogen stays in an atomic form for a significant time scale ($\gtrsim 10^5$ yr) in molecular clouds. Therefore, we next investigate the dependence of PN and PO abundances on the initial abundance of N atoms.

Figure 2.4 shows the temporal variation of PN, PO, and N atoms with various initial N atom abundances. The elemental abundance of nitrogen is kept constant; in a model with

high N atom abundance, the initial N_2 abundance is low. As expected, PN abundance is significantly increased, whereas PO abundance is lowered, if the initial N atom abundance is high. The abundances of other P-bearing species (P atom, PH, and PH_3) do not change significantly from those shown in Figure 2.2. N atom decreases at $t = 10^4 - 10^5$ yr (Figure 2.4 c); it is converted to N_2 by the following reactions

$$\mathrm{N + OH \rightarrow NO + H} \tag{2.8}$$

$$\mathrm{N + NO \rightarrow N_2 + O} \tag{2.9}$$

$$\mathrm{NO + NH_2 \rightarrow N_2 + H_2O.}$$

Then PN is converted back to PO as N atom decreases (Figure 2.3).

If the initial N atom abundance is 1.0×10^{-6}, the observed abundance of PN is reproduced on a relatively limited time scale $\sim 10^4$ yr, but PO abundance exceeds the observed upper limit. On the other hand, if the initial N atom abundance is 1.0×10^{-5}, PO abundance is consistent with the upper limit for a longer time scale, but PN abundance slightly exceeds the observed abundance ($(1-3) \times 10^{-10}$ relative to n_{H}) at $t \sim 10^4$ yr. We note here that these abundances of P-bearing species are proportional to the initial PH_3 abundance. In the current calculation, we assumed the initial PH_3 abundance of 1.2×10^{-8} following Charnley & Millar (1994). However, this assumption is rather arbitrary; Charnley & Millar (1994) did not compare their PN abundance with observation quantitatively, because the abundance estimates in hot cores were uncertain due to beam dilution and difficulty in estimating the H_2 column density. Thus far, there are no direct observational constraints on PH_3 abundance. Dot-dashed lines in Figure 2.4 show the temporal variation of PO and PN with the initial PH_3 abundance of 1.2×10^{-9} and N atom abundance of 10^{-5}; both PN and PO abundances are consistent with the observation.

We also note that the initial form of desorbed phosphorus is not necessarily PH_3, since there are no observational constraints on P in solids. Our results do not change if P is desorbed as P atoms, instead of PH_3, because P atoms are on the path to PN in the chemical network (see Figure 2.3).

2.3.2 Model B

In Model A and Figure 2.3, we can see that N atoms, O atoms, and protonated water are major reactants with P-bearing species. This indicates that P chemistry may depend on the initial abundances of water and O atoms, as well as on the N atom abundance. In order to check the dependence of P chemistry on initial molecular abundances, here we set the initial abundances by calculating molecular evolution in a molecular cloud condition, $n(H_2) = 1.0 \times 10^4$ cm^{-3} and $T = 10$ K (Figure 2.5). We adopt the molecular abundance at 1×10^5 yr as the initial abundance for the shock model. Ice mantle species are assumed to be desorbed to the gas phase as in Model A. We assume that phosphorus is totally depleted in the solid phase in molecular clouds, but a fraction (1.2×10^{-8} relative to hydrogen nuclei) of P is desorbed to the gas phase in atomic form via sputtering in the shock.

Figure 2.6 (a) shows the temporal variation of P-bearing species in the C shock model. Major chemical reactions of P-bearing species are mostly the same as in Model A. Since N atoms are as abundant as 10^{-5} initially, PN becomes abundant, whereas PO is depleted at $t \sim 10^4$ yr. If we adopt the abundances at $t = 1 \times 10^6$ yr in the molecular cloud as initial conditions for the shock chemistry, PO abundance exceeds the observed upper limit at $t \sim 10^4$ yr (Figure 2.6b), because the initial N atom abundance is low ($\sim 7.0 \times 10^{-7}$).

As in Model A, the abundances of P-bearing species are proportional to the assumed elemental abundance of P in the gas phase. If we adopt the molecular cloud abundance at 10^5 yr and the initial P atom abundance of $\sim 3 \times 10^{-9}$, our PN and PO abundances become consistent with the observation at $\sim 10^4$ yr.

2.4 Discussion 1 : Differences between our results and those of Charnley & Millar (1994)

In our model, PN becomes abundant *only* if initial N atom abundance is high ($\gtrsim 10^{-5}$). In the hot core model of Charnley & Millar (1994), on the other hand, abundant PN is formed in $\sim 10^4$ yr even though N is all in N_2 initially. Why do we need abundant N atoms? Is it due to the difference in physical models (hot core vs. shock) or chemical reaction networks? We note that Charnley & Millar (1994) used the network model of UMIST91 (Millar et al.

1991). Since reaction rate coefficients have been updated significantly since UMIST91, it is worth investigating how our network model differs from UMIST91, and if our conclusion, that there is high N atom abundance in pre-shock gas, sensitively depends on the reaction network model.

2.4.1 Comparison between chemical network models

In order to compare our network model with UMIST91, we calculated the same hot core model as Charnley & Millar (1994). We adopted the initial abundance in their Table 2; it is essentially similar to our initial condition of Model A with abundant N_2 and saturated molecules such as H_2O. Temperature and density are set to T=100 K and $n(H_2) = 10^7$ cm^{-3}.

The result is shown in Figure 2.7 (a). At $t \simeq 10^4 - 10^5$ yr, PN abundance is much lower, and PO abundance is much higher than that in Charnley & Millar (1994), in which PO decreases and PN abundance reaches several 10^{-9} at $t \sim 10^4$ yr (see Figure 1 of Charnley & Millar 1994). Nitrogen atoms, which are needed to form PN, are not abundant until $t \sim$ several 10^5 yr; although N atoms are formed by $N_2 + He^+$, their abundance is suppressed by reactions (2.8) and (2.9). Although N atom abundance is not shown in Charnley & Millar (1994), it might be higher than in our model. Since N atom abundance depends on N-chemistry and O-chemistry (see reactions (2.8) and (2.9)), we compared the rate coefficients of major N- and O- reactions. Table 3 lists several reactions that we found to have different rate coefficients in our network and UMIST91. For example, the rate coefficient of

$$CO + OH \rightarrow CO_2 + H \tag{2.10}$$

is 500 times higher in UMIST91 than in our model at T=100K; the rate coefficient in UMIST91 is adopted from Smith (1988), whereas our rate coefficient is from Frost et al. (1993). For reactions that are not included in UMIST91, we put 0 in the column of A parameter of "UMIST91" in Table 2.3. It is natural that most of the reactions listed in Table 2.3 are neutral-neutral reactions, whose rate coefficients are hard to measure at low temperatures in laboratories.

We adopted the rate coefficients of UMIST91 for the reactions in Table 3 (hereafter,

modified network model) and calculated the hot core chemistry of Charnley & Millar (1994) (Figure 2.7b). Now, the temporal variation of P-bearing species is more similar to that in Charnley & Millar (1994) than to that in Figure 2.7 (a). We can conclude that there are differences in N-chemistry and O-chemistry between our network and UMIST91, which significantly affect P-chemistry.

2.4.2 Shock chemistry with the modified network model

Using the modified network model, we calculated the C-shock model to see how the evolution of P-bearing species differs from our original model. The initial abundances are the same as in Model A. Figure 2.8 shows the PN and PO abundances with various initial N atom abundances ($0, 1.0 \times 10^{-7}, 1.0 \times 10^{-6}$, and 1.0×10^{-5}). Although these results are slightly different from those in Figure 2.4, our original conclusion stands: PN and PO abundances become consistent with the observed value and the upper limit *only* if N atom abundance is as abundant as $\gtrsim 10^{-5}$.

2.4.3 Dependence of hot core model on physical parameters

Using the modified network model, PN becomes abundant at $\sim 10^4$ yr in the hot core model (as in Charnley & Millar 1994) even if the initial N atom abundance is zero. In the shock model, on the other hand, we still need initially high N atom abundance to make PN abundant at $\sim 10^4$ yr. Since we are now comparing the two models with the same chemical reaction network, the difference should be attributable to the physical conditions. In the C-shock model for L1157 B1, density ($n(\mathrm{H_2}) = 10^4$ cm^{-3}) is much lower than that in the hot core model ($n(\mathrm{H_2}) = 10^7$ cm^{-3}), and the temperature varies temporally from 10 K to 1000 K, whereas the hot core model has a fixed temperature (100 K). In the following we calculate hot core models with various densities and temperatures in order to determine density, temperature, or both affect the P chemistry. We use the modified reaction network and the initial conditions shown in Table 2 in Charnley & Millar (1994).

Figure 2.9(a) shows the PN abundance in hot core models of $T = 100$ K with the gas densities of $n(\mathrm{H_2}) = 1.0 \times 10^4$ cm^{-3}, 1.0×10^5 cm^{-3}, and 1.0×10^7 cm^{-3}. We can see that PN is formed in shorter time scales at higher densities. In general, chemical reactions

proceed faster at higher densities. Whereas the collisional time scale of gaseous particles is proportional to n^{-1}, the chemical time scale's dependence on density is weaker than n^{-1}, because the ion-molecule reactions play major roles in the reaction network and because the ionization degree is proportional to $n^{-1/2}$.

Figure 2.9 (b) shows the PN abundance in hot core models of $n(H_2) = 1.0 \times 10^7$ cm^{-3} with T = 10 K, 30 K, 50 K, and 100 K. At lower temperatures, PN is less abundant, because the N atom is destroyed by the reaction with the OH (reaction(2.8)). Figure 2.9(c) shows the OH abundance in the same models as in Figure 2.9(b). OH increases with time at low temperatures (10 K and 30 K), whereas at $T = 100$ K, OH is destroyed by the reaction (2.10), which has an activation barrier of 390 K in UMIST91. We note that in the C-shock model (Figure 1), temperature initially increases to $\sim$ 1000 K, but decreases to $\sim$ 10K after several 10^3 yrs, when the OH abundance increases and hampers the formation of PN.

From these discussions, we can conclude that both high density and high (constant) temperature help to make PN abundant in the hot core model, whereas in the C-shock model, we need high N atom abundance in the pre-shock gas in order to make PN abundant at 10^4 yr.

2.5 Discussion 2 : Dependence on shock parameters

So far, we have adopted the C-shock model of $n(H_2)$=1.0$\times 10^4$ cm^{-3} and v = 20 km s^{-1} (Figure 2.1). In this section, we investigate the dependence of P-chemistry on C-shock parameters: pre-shock density and velocity. We use our original reaction network and adopt the initial conditions in Model A. The initial N atom abundance is 1.0×10^{-5}. Figure 2.10 shows the temporal variation of neutral, ion, and electron temperatures, H_2 density, and neutral and ion velocities in two C-shock models: (a, c) the pre-shock density $n(H_2) = 10^4$ cm^{-3} and velocity v = 40 km s^{-1}, and (b, d) $n(H_2) = 10^5$ cm^{-3} and v = 20 km s^{-1}. The peak temperature is higher in the model with higher velocity, whereas the cooling time is shorter in the model with higher pre-shock density.

Figure 2.11 (a) shows the temporal variation of P-bearing species in the model of $n(H_2) = 10^4$ cm^{-3} and v = 40 km s^{-1}. Since the peak temperature is higher than the model

with $v = 20$ km s^{-1}, N atoms are depleted in the high-temperature region ($T \sim 2000$K) by

$$H_2 + N \rightarrow NH + H, \tag{2.11}$$

which has an energy barrier of 1.66×10^4 K. Then, PN is less abundant and PO is more abundant than Figure 2.4 (b). NH is further hydrogenated to NH_3 by

$$NH + H_2 \rightarrow NH_2 + H \tag{2.12}$$

$$NH_2 + H_2 \rightarrow NH_3 + H, \tag{2.13}$$

which also have activation barriers. At high temperatures, H atoms increase due to collisional dissociation of H_2, which starts the back reactions of (2.11)-(2.13). However, back reactions are not efficient enough to stop the decline of N atom abundance. Figure 2.11 (b) shows the same shock model but with the initial N atom abundance of 7.46×10^{-5}; nitrogen is initially all in atomic form. PN is more abundant than PO at $\sim 10^4$ yr. If we reduce the initial PH_3 abundance by a factor of a few, PO abundance can be marginally lower than the upper limit, whereas PN abundance is in the range of observed values.

Figure 2.11 (c) shows, on the other hand, the temporal variation of P-bearing species with the pre-shock density $n(H_2)$=1.0×10^5 cm^{-3} and velocity $v = 20$ km s^{-1}. The results are similar to those in Figure 2.4; PN is abundant and PO is depleted at $t \sim 10^4$ yr.

In summary, the observed abundances of PN and PO are reproduced in the C-shock models if the peak temperature is less than $T < 2000$ K. In the shock model with higher peak temperatures, only marginal agreement is found with an extremely high initial N atom abundance.

2.6 Conclusions

In this work, we have calculated the phosphorus chemistry in 1D steady-state C-shock models to examine how PN is formed and why PO is not detected in the shocked region L1157 B1. We found that PN and PO abundances in our model become consistent with the observation, if the following conditions are satisfied:

- a fraction of phosphorus, $\sim 10^{-9}$ relative to hydrogen, is desorbed from the grain to the gas phase as PH_3 or P atom via sputtering in the shock

- initial N atom abundance is high ($\gtrsim 10^{-5}$)
- the peak temperature of the shocked gas is < 2000 K.

We have also compared our reaction network model with UMIST91, which is adopted in the hot core model of Charnley & Millar (1994). Phosphorus chemistry sensitively depends on the abundance of N atoms, which in turn depends on N- and O-chemistry. We identified several neutral-neutral reactions with different rate coefficients in our network models and UMIST91, and these reactions significantly affect the P-chemistry. We confirmed that our conclusion — a high abundance of N atoms in the pre-shock gas is needed to make PN abundant — is valid even if we modify the rate coefficients of these reactions to those of UMIST91. Furthermore, our results indicate that, even in hot core models, high N atom abundance is needed to make PO less abundant than PN at $t \sim 10^4$ yr, if we adopt our updated network instead of UMIST91.

Species	Abundance	Species	Abundance	Species	Abundance	Species	Abundance
H_2	0.5	CO_2	3.0×10^{-6}	CH_3OH	2.0×10^{-7}	C_2H_4	5.0×10^{-9}
He	0.1	H_2CO	2.0×10^{-6}	H_2S	1.0×10^{-7}	C_2H_5OH	5.0×10^{-9}
H_2O	2.8×10^{-4}	O_2	1.0×10^{-6}	OCS	5.0×10^{-8}	C_2H_6	5.0×10^{-9}
CO	1.3×10^{-4}	NH_3	6.0×10^{-7}	Si	3.6×10^{-8}	Fe^+	2.4×10^{-8}
H	5.0×10^{-5}	C_2H_2	5.0×10^{-7}	PH_3	1.2×10^{-8}	H_3^+	1.0×10^{-9}
N_2	3.7×10^{-5}	CH_4	2.0×10^{-7}	S	5.0×10^{-9}	H^+	1.0×10^{-11}
						He^+	2.5×10^{-12}

Table 2.1: Initial molecular abundances relative to hydrogen nuclei in Model A

Species	Abundance	Species	Abundance	Species	Abundance
H_2	5.0×10^{-1}	C^+	1.36×10^{-4}	S^+	1.55×10^{-7}
He	1.0×10^{-1}	N	7.46×10^{-5}	Si^+	3.6×10^{-8}
O	4.18×10^{-4}	H	5.0×10^{-5}	Fe^+	2.4×10^{-8}

Table 2.2: Initial abundances in the molecular cloud model for Model B

	OSU				UMIST91			
reaction	A	B	C	$k(T=100$ K$)$[2][1]	A	B	C	$k(T=100$ K$)$
$CO + OH \rightarrow CO_2 + H$	2.81 (-13)[3][2]	0	176	4.8 (-14)	3.1 (-10)	-1.15	390	2.2 (-11)
$O + NH_2 \rightarrow NO + H_2$	1.0 (-11)	0	0	1.0 (-11)	0	-	-	-
$O + NH_2 \rightarrow NH + OH$	2.0 (-11)	0	0	2.0 (-11)	3.5 (-12)	0.5	0	2.02 (-12)
$O + NH \rightarrow NO + H$	1.16 (-10)	0	0	1.16 (-10)	1.73 (-11)	0.5	0	1.0 (-11)
$O + PH \rightarrow PO + H$	1.0 (-10)	0	0	1.0 (-10)	4.0 (-11)	0	0	4.0 (-11)
$HPO^+ + H_2O \rightarrow H_3O^+ + PO$	–[4]3	–[5]3	–[6]3	3.9 (-9)	1.0 (-9)	0	0	1.0 (-9)
$N + NO \rightarrow N_2 + O$	3.0 (-11)	-0.6	0	5.8 (-11)	3.4 (-11)	0	0	3.4 (-11)
$N + OH \rightarrow NO + H$	7.5 (-11)	-0.18	0	9.14 (-11)	5.0 (-11)	0.5	0	2.89 (-11)
$N + CH_3 \rightarrow H_2CN + H$	8.6 (-11)	0	0	8.6 (-11)	0	-	-	-
$O + OH \rightarrow O_2 + H$	3.5 (-11)	0	0	3.5 (-11)	7.9 (-11)	0	0	7.9 (-11)
$O + HNO \rightarrow OH + NO$	3.8 (-11)	0	0	3.8 (-11)	1.44 (-11)	0.5	0	8.31 (-12)
$O + NH_2 \rightarrow HNO + H$	8.0 (-11)	0	0	8.0 (-11)	3.2 (-12)	0	0	3.2 (-12)
$CH_5O^+ + e \rightarrow CH_3 + OH + H$	4.64 (-7)	-0.67	0	9.69 (-7)	0	-	-	-
$CH_5O^+ + e \rightarrow CH_3 + H_2O$	8.19 (-8)	-0.67	0	1.71 (-7)	0	-	-	-
$CH + H_2 \rightarrow CH_3$	3.25 (-17)	-0.6	0	6.28 (-17)	0	-	-	-
$CH_3OCH_4^+ + e \rightarrow CH_3 + CH_4 + O$	1.5 (-7)	-0.5	0	2.6 (-7)	0	-	-	-
$CH_3OCH_4^+ + e \rightarrow CH_4O + CH_3$	1.5 (-7)	-0.5	0	2.6 (-7)	0	-	-	-
$O + C_3H_3 \rightarrow C_2H_2 + HCO$	2.31 (-10)	0	0	2.31 (-10)	0	-	-	-
$O + CH_2 \rightarrow HCO + H$	5.01 (-11)	0	0	5.01 (-11)	1.44 (-11)	0.5	2000	1.71 (-20)
$H + HCO \rightarrow H_2 + CO$	1.5 (-10)	0	0	1.5 (-10)	3.0 (-10)	0	0	3.0 (-10)
$PO + N \rightarrow PN + O$	3.0 (-11)	-0.6	0	5.8 (-11)	3.4 (-11)	0	0	3.4 (-11)

Table 2.3: List of reactions with different rate coefficient in our model and UMIST91 which affect the P-chemistry. Rate coefficients are given as a function of A, B, and C: $k = A(T/300)^B \exp(-C/T)$.

[1]Rate coefficient at $T = 100$ K.

[2]$a(-b)$ means $a \times 10^{-b}$.

[3]The rate coefficient in OSU model is calculated using equations (3), (5) - (7) of Harada et al. (2010)

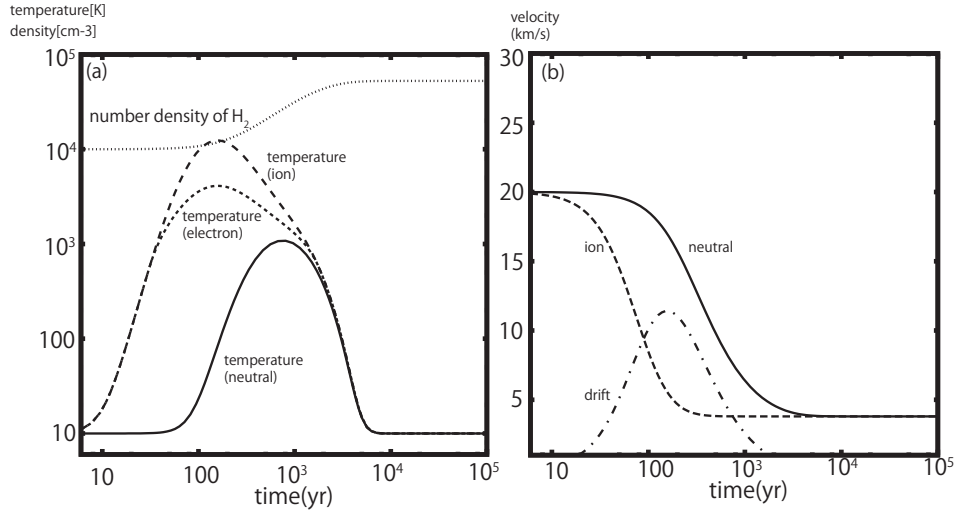

Figure 2.1: (a) Temporal variation of neutral, ion, and electron temperatures and H_2 density in the C-shock model with pre-shock density $n(H_2) = 1.0 \times 10^4$ cm^{-3} and velocity $v = 20$ km s^{-1}. (b) Temporal variation of the neutral and ion velocities in the C-shock model. Velocity is in the frame co-moving with the shock front. Dot-dashed line depicts the ion-neutral drift speed ($|u_{\rm i} - u_{\rm n}|$).

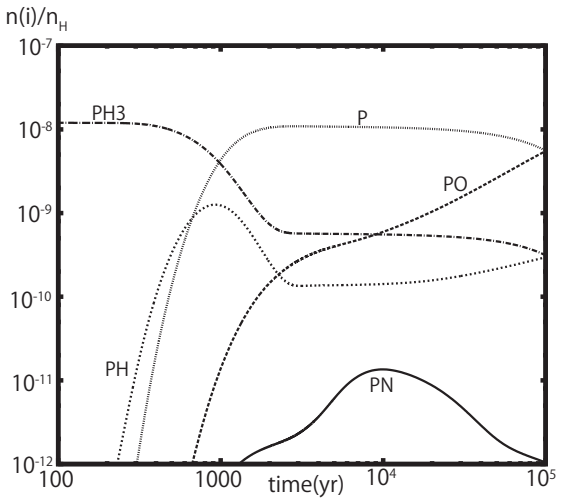

Figure 2.2: Temporal variation of P-bearing species in Model A. Initial N atom abundance is set to zero.

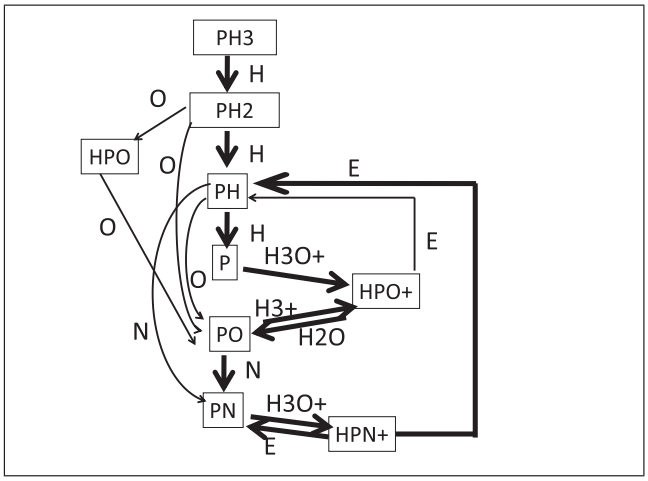

Figure 2.3: Reaction network of P-bearing species in the shocked gas.

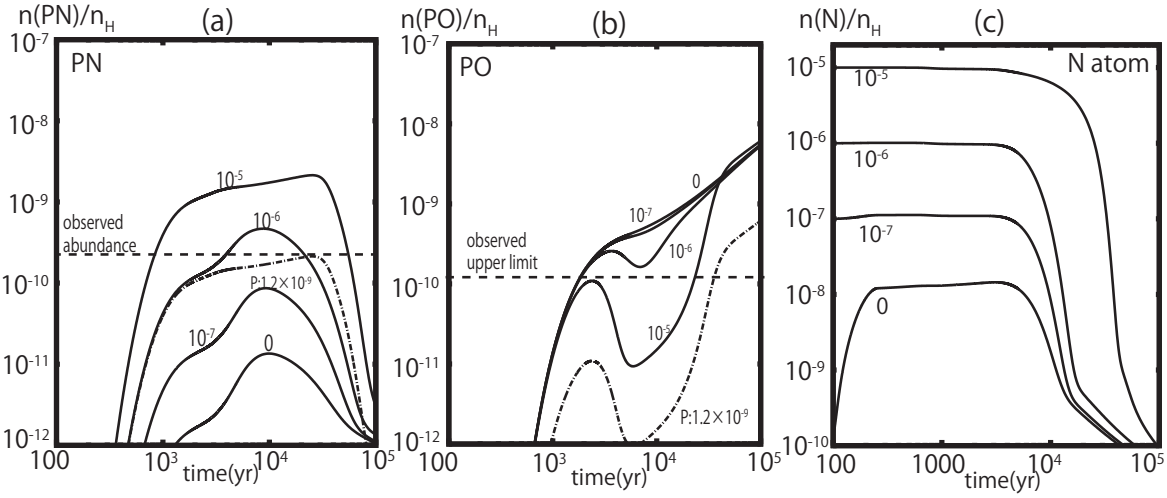

Figure 2.4: PN, PO, and N atom abundances in Model A with various initial N atom abundances, which are each attached to a line. Dot-dashed lines represent PN and PO abundances with the initial PH_3 abundance of 1.2×10^{-9} and N atom abundance of 10^{-5}.

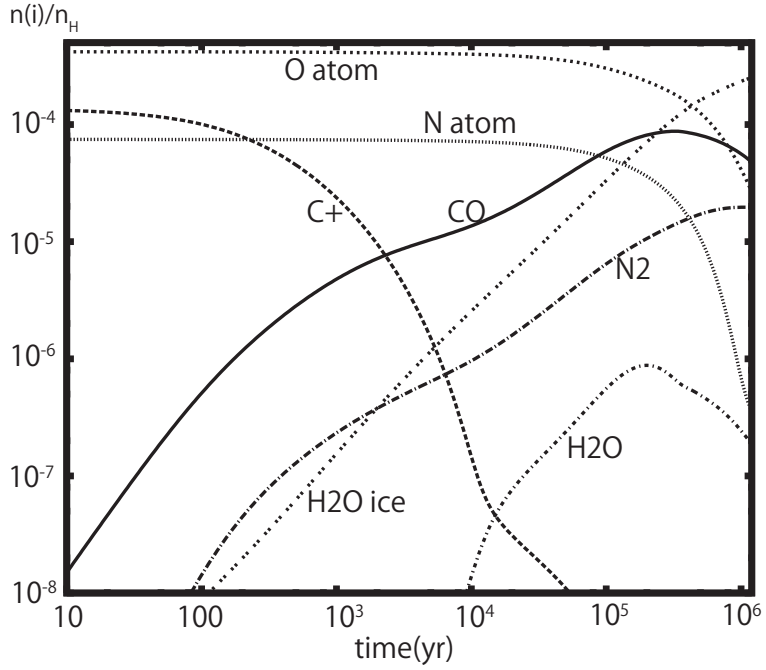

Figure 2.5: Molecular evolution in the molecular cloud condition, $n_{\rm H} = 2.0 \times 10^4$ cm^{-3} and $T = 10$ K.

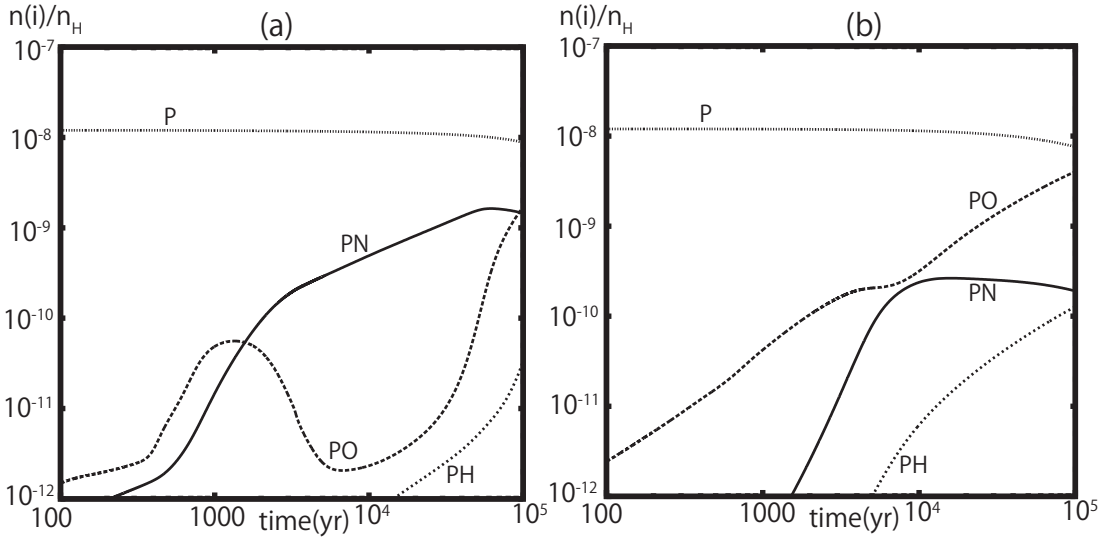

Figure 2.6: Temporal variation of P-bearing species in Model B. We adopt the molecular cloud abundances at (a) $t = 1 \times 10^5$ yr and (b) $t = 1 \times 10^6$ yr as the initial conditions of shock chemistry. P atoms are assumed to be desorbed to the gas phase by sputtering in the shock.

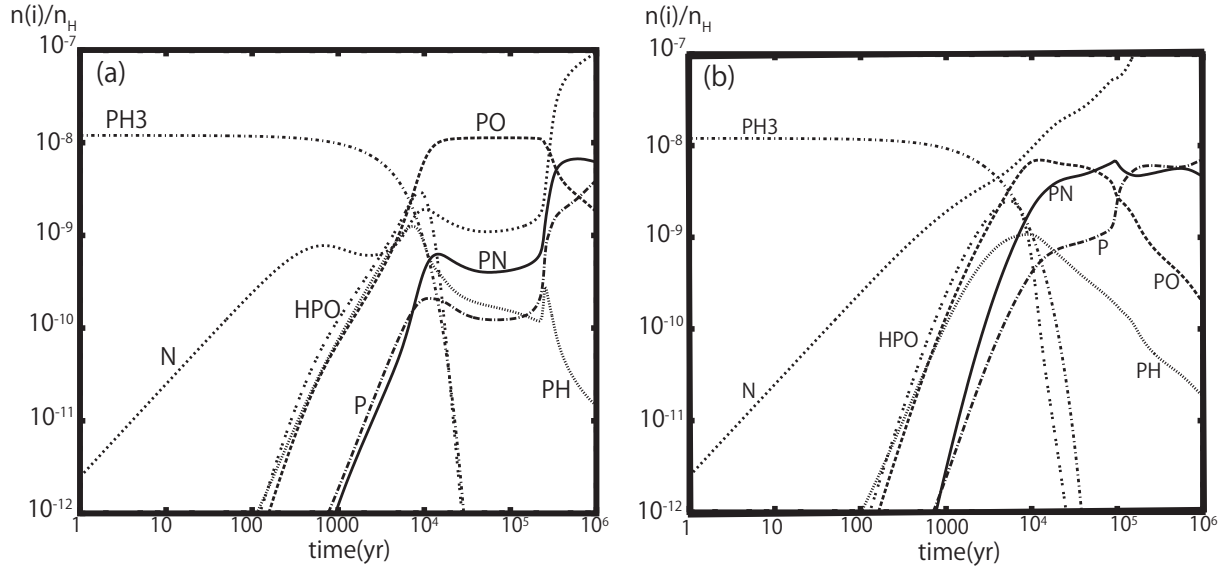

Figure 2.7: Temporal variation of P-bearing species in the hot core model of T=100K and $n_{\rm H}$=2.0×10^7 cm^{-3}. We use our original network model in (a) and the modified network model in (b).

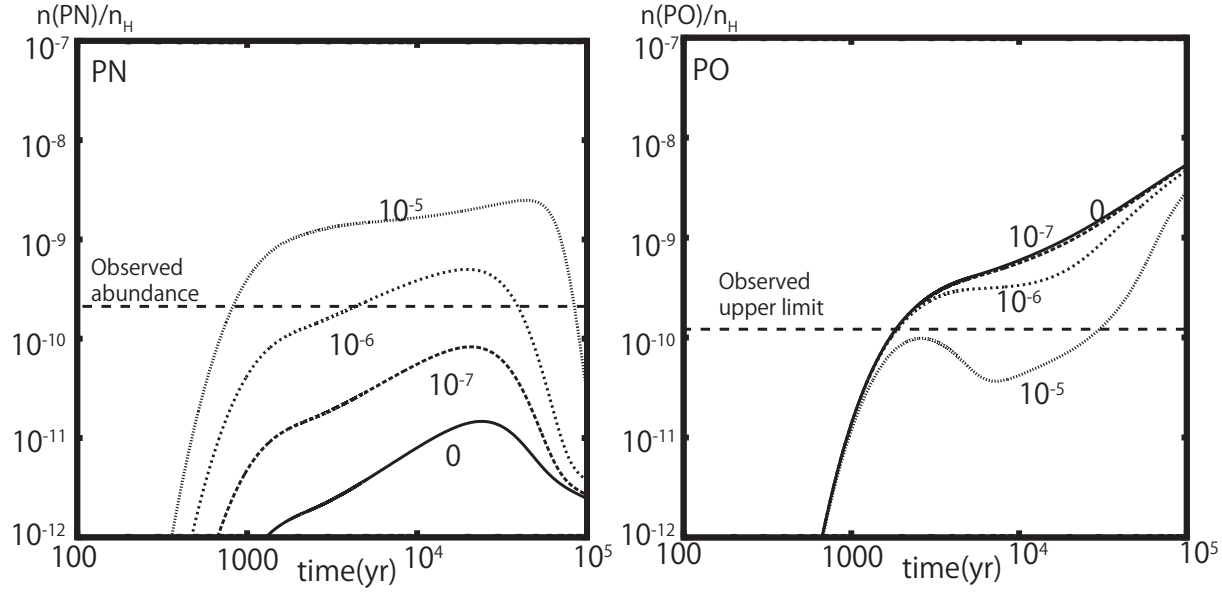

Figure 2.8: PN and PO abundances in the shock model as shown in figure 2.4 but with the modified network model.

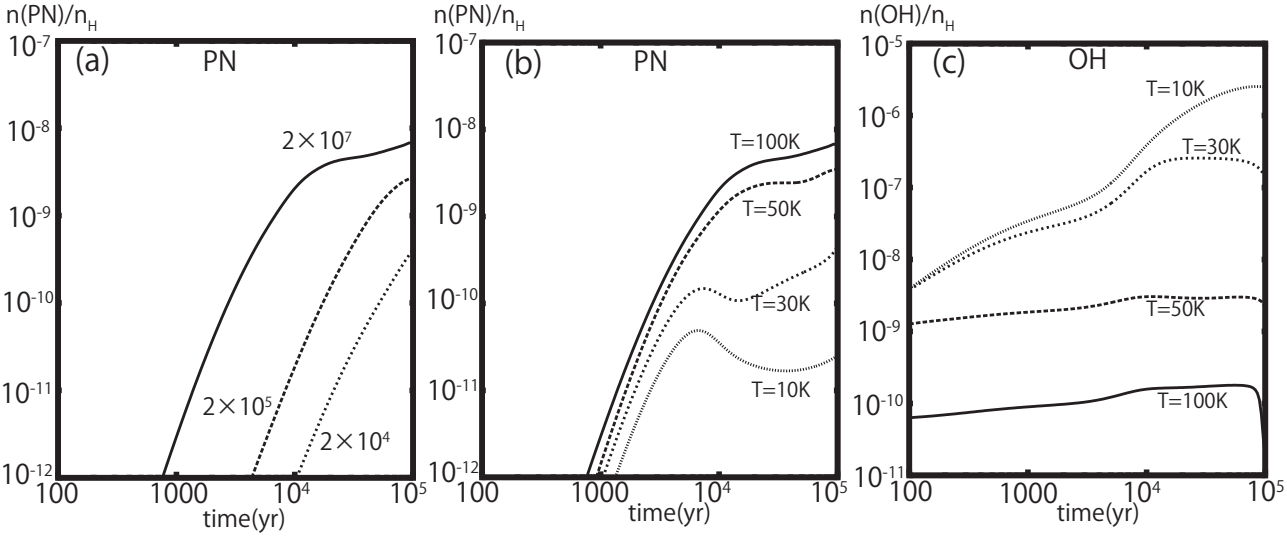

Figure 2.9: (a) Dependence of PN abundance on gas density ($n_{\rm H}$=2.0×10^7, 2.0×10^5, 2.0×10^4 cm^{-3}), and (b, c) dependence of PN and OH abundances on temperatures (T=10, 30, 50, 100K) in hot core model.

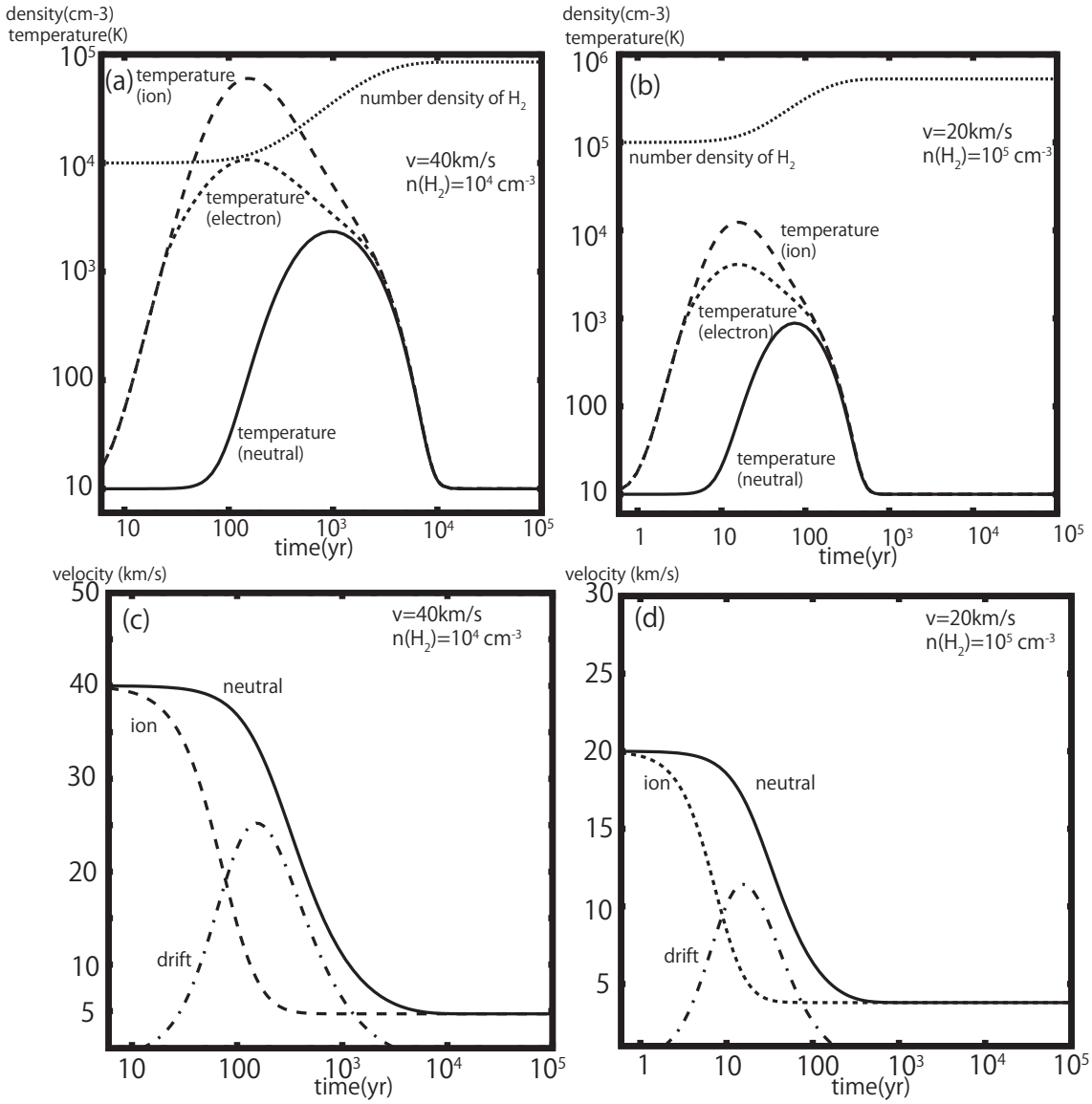

Figure 2.10: Temporal variation of temperature and density in the C-shock model with (a) pre-shock density $n(\mathrm{H_2}) = 1.0 \times 10^4$ cm^{-3} and velocity $v = 40$ km s^{-1}, and (b) $n(\mathrm{H_2}) = 1.0 \times 10^5$ cm^{-3} and velocity $v = 20$ km s^{-1}. (c-d) Temporal variation of the neutral and ion velocities in the two C-shock models.

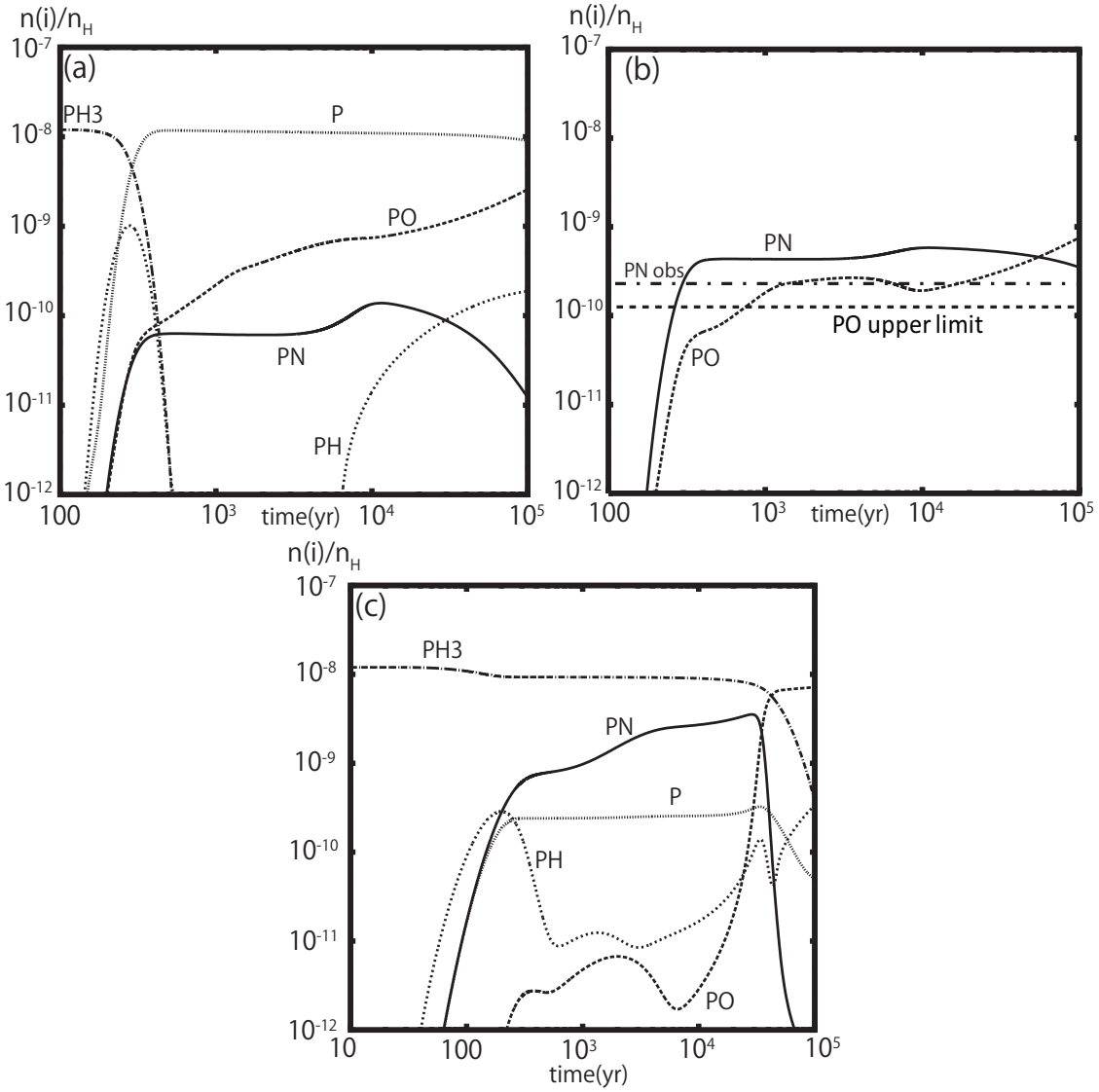

Figure 2.11: Temporal variation of P-bearing species in the C-shock model with pre-shock density $n_{\rm H} = 2.0 \times 10^4$ cm^{-3} and velocity $v = 40$ km s^{-1} (a-b), and $n_{\rm H} = 2.0 \times 10^5$ cm^{-3} $v = 20$ km s^{-1} (c). Initial N atom abundance is 1.0×10^{-5} in (a) and (c), whereas it is 7.46×10^{-5} in (b). Dashed and dot-dashed lines in panel (b) depict the observed PN abundance and upper limits on PO abundance, respectively.

Chapter 3

Evaporation of grain-surface species by shock waves in proto-planetary disk

3.1 Introduction

Volatile molecules such as H_2O and CO_2 are important ingredients of planetary systems. They are major carrier of volatile elements, oxygen and carbon, and could make atmosphere and ocean. Since these molecules are readily found in interstellar ice in molecular clouds, one open question is if and how they are delivered to protoplanetary disks and then to planets. In our solar system, relative abundances of volatiles to water in comets are observed to be similar to those in interstellar ice, which suggests that the interstellar ice could have been raw material of Solar system, at least in comet forming regions (Mumma & Charnley 2011).

In recent years, theoretical models of chemistry in protostellar cores and forming disks have been constructed by several groups. As the infall material enters the warm central regions, complex organic molecules can be formed via grain-surface reactions on warm grains (Garrod & Herbst 2006; Herbst & Van Dishoeck 2009). In spherical symmetric models, molecules are sublimated at their sublimation temperatures, forming an onion-like distribution of molecular abundances in the envelope (e.g. Rodgers & Charnley 2003; Aikawa et al. 2008, 2012; Visser et al. 2009, 2011). In models of disk formation, the temperature distribution is not spherically symmetric, and the chemical composition of an infalling fluid parcel depends on its orbit; if the fluid parcel experiences only low temperatures, a

significant amount of interstellar ice can survive to reach the disk (Visser et al. 2009, 2011).

Since the infalling flow is supersonic, accretions onto protoplanetary disks are accompanied by a shock wave. The kinetic energy of the bulk flow is converted to the thermal energy. While the gas is decelerated by the enhanced pressure at the shock front, dust grains fall into the disk, and ice mantles on grain surfaces are sublimated by gas-drag heating (e.g. Hood & Horanyi 1991; Lunine et al. 1991; Neufeld & Hollenbach 1994) and/or sputtered by collisions with gas particles (e.g. Barlow 1978; Draine & Salpeter 1979; Jiménez-Serra et al. 2008). Lunine et al. (1991) investigated sublimation of volatiles by the drag heating in the primitive solar nebula. They showed that 90 % of water ice is sublimated by the drag heating at the radius of 30 AU. The water vapor then re-condenses onto grain surface, because the solar nebular is cold. Neufeld & Hollenbach (1994), on the other hand, performed more general calculations of dense molecular shocks with pre-shock density $10^{7.5} - 10^{12}$ cm^{-3} and velocity $5 \leq v \leq 100$ km s^{-1}. They obtained grain vaporization criteria for various grain materials such as water ice, organic refractory materials, silicate and iron.

Chemistry in these protostellar cores and disk forming stages are now intensively observed with ALMA. Spatial distributions of molecules start to be revealed towards template protostellar objects IRAS 16293 (Pineda et al. 2012; Zapata et al. 2013) and L1527 (Sakai et al. 2014). Sakai et al. (2014) detected SO gas towards L1527. The position velocity diagram indicates that the SO is located in a ring region at the radius of $\sim$ 100 AU. This ring structure, together with the warm temperature ($\sim$ 70 K) derived from the LVG analysis, suggest that SO is tracing accretion shock. According to the theoretical models of protostellar cores (Aikawa et al. 2012), SO ice could be abundant in infalling material. When the dust temperature gets higher than $\sim$ 60 K in the shock, SO can be sublimated to the gas phase. The warm SO ring is also observed towards L1489 IRS (Yen et al. submitted to ApJ).

If the SO emission is really tracing the accretion shock onto forming disk, it has significant impacts on studies on physics and chemistry of disk formation. Since the accretion flux is the largest around the temporal centrifugal radius, SO emission could tell the size of the forming disk. Chemical composition of the infall material might be altered at the ac-

cretion shock. Although Lunine et al. (1991) predicted that the vapor simply recondenses in the disk, they did not include chemical reactions in their model. It is thus important to confirm that SO is really originated in accretion shock, rather than, e.g. sublimation due to stellar heating. While observers are trying higher spatial resolution observation of the SO emission, theoretical models on accretion shock should be revisited in the context of disk formation.

In this work, we investigate the desorption of volatile species in the accretion shock onto protoplanetary disks. Our motivations are twofold; we investigate (1) if the SO emission detected toward the protostellar objects is consistent with accretion shock model and (2) what other molecules can be detected in accretion shock. We calculate the physical structure of one-dimensional J-shock with pre-shock gas density and velocity relevant to the disk formation. Then we evaluate the drag heating of grains and a fraction of volatile molecules desorbed to the gas phase via thermal desorption and sputtering. While Neufeld & Hollenbach (1994) investigated a wide range of pre-shock velocity, we concentrate on low pre-shock velocities ≤ 10 km s^{-1} and investigate desorption of various volatile molecules, which were not included in Neufeld & Hollenbach (1994), in addition to water. Based on the 1-D shock model, we discuss the origin of SO emission detected towards forming disks with ALMA. This paper is organized as follows. In 3.2, we describe our physical and chemical models. In 3.3, we show the resultant shock structure, fraction of volatiles sublimated as a function of pre-shock density and velocity. We evaluate the column density of warm molecules in post-shock region and compare them with observation. Finally, we summarize our results in 3.4.

3.2 The model

We investigate the accretion shock onto protoplanetary disk using 1D plane-parallel model. Figure 3.1 schematically shows the configuration of our model. We consider a collision of gas flow with rigid wall. This configuration also corresponds to a face-on collision between two gas flows with the same density. In this work, our calculations consist of two steps. Firstly, we calculate physical structure of the shock, i.e. density, temperature and velocity of gas. Secondly, we calculate dust velocity, temperature and desorption of ice mantles in

the post shock region. We explain these calculation processes in the following subsections in detail.

3.2.1 Structure of 1D shock

We preform one dimensional hydrodynamic simulation. We solve the conservation of mass, momentum and energy:

$$\partial_t U(t,x) + \partial_x F_x = S$$

$$U = (\rho, \rho v_x, E)$$

$$F_x = \begin{pmatrix} \rho v_x \\ \rho v_x^2 + p \\ (E+p)v_x \end{pmatrix}$$

$$S = \begin{pmatrix} 0 \\ 0 \\ -\rho\,\Lambda \end{pmatrix}$$

$$E = \frac{p}{\gamma - 1} + \frac{\rho v_x^2}{2} \quad ,$$

where ρ, v_x, p, γ and Λ are the gas mass density, velocity, thermal pressure, ratio of specific heat, and cooling rate per unit mass, respectively. There is no external heating in our model; we assume that infalling flow is well-shielded from UV and X rays. The gas is heated only by shock heating.

We use an operator-splitting technique to solve these equations, which are split into two parts: (1) ideal hydrodynamics, and (2) cooling (e.g., Inoue & Inutsuka 2008). Ideal hydrodynamics is calculated by the second-order Godunov method with Lagrangian coordinates (Van Leer, 1979). We solve the exact Riemann problem iteratively at each grid cell interface to calculate numerical fluxes, and determine the position of grid cell interface in the next time step. The energy equation

$$\frac{\partial E}{\partial t} = -\rho\,\Lambda$$

is solved by the second-order explicit method.

In this work, we consider high density gas ($n_{\rm H} \geq 10^6$ cm^{-3}) accreting onto protoplanetary disk. In such high densities, gas is cooled by gas-dust collisional cooling. We adopt

the formula of gas-dust collisional cooling per unit volume by Hood & Horanyi (1991),

$$\rho\,\Lambda = \frac{1}{2}\pi^{0.5} a_{\rm dust}^2 n_{\rm dust}\rho_{\rm gas}(T_{\rm gas}-T_{\rm dust})\frac{\gamma+1}{\gamma-1}\left(\frac{2k_{\rm bol}}{m_{\rm gas}}\right)^{1.5} T_{\rm gas}^{0.5}, \tag{3.1}$$

where $a_{\rm dust}$, $n_{\rm dust}$, $k_{\rm bol}$ and $m_{\rm gas}$ are grain radius, number density of dust grain, Boltzmann constant and mean mass of gas particle, respectively. In this work, we set $a_{\rm dust} = 0.1$ μm, which is a typical grain radius in interstellar clouds (Tielens 2005), and mean mass of gas is set to be $m_{\rm gas} = 1.67\times10^{-24}\left(\frac{2n_{\rm H_2}+4n_{\rm He}}{n_{\rm H_2}+n_{\rm He}}\right) \sim 3.9\times10^{-24}$ g. $T_{\rm dust}$ is determined by the balance between heating and cooling; gas-grain energy transfer and cooling by thermal emission of dust (see section 2.2). At this stage, we neglect the relative velocity between gas and dust; the heating rate of dust grains is given by equation (3.1). The dust temperature derived here is slightly different from the value obtained in section 2.2., where we take into account the gas-dust drag. But the difference is so small that it does not affect the gas temperature. We neglect other cooling mechanisms such as CO rotational cooling, which are less efficient than gas-dust cooling at $n_{\rm H} \geqq 10^7$ cm^{-3}.

The time step of the integration is set to be small enough to satisfy the Courant-Friedrichs-Lewy (CFL) condition: $0.03\times\tau_{cool}$, where τ_{cool} is the cooling time. In this work, we set the minimum and initial gas temperature to be 20K. We explore the parameter space of pre-shock number density of hydrogen nuclei $n_{\rm H} = 10^6, 10^7, 10^8$ and 10^9 cm^{-3}. We adopt these temperature and density for pre-shock gas referring to the recent three dimensional SPH simulation of disk formation and evolution with radiation transfer (Tsukamoto et al. 2013). The accretion velocity $V_{\rm acc}$ range from 1 km s^{-1} to 10 km s^{-1}, which corresponds to the free fall velocity at $r \gtrsim 15$AU around a Solar mass protostar. These velocities are chosen considering the spatial resolution of ALMA observation. The highest spatial resolution of line observation by ALMA is of order 0.1 second. If we consider the nearest star forming regions such as Taurus, spatial resolution is about 15 AU. In this work, our numerical domain varies from 1.0×10^{-3} pc to 2.0×10^{-6} pc depending on the model parameters (see Table 3.1). The numerical domain is divided into 450 grid cells with equal intervals. Although our hydrodynamics code is time-dependent, we use it to obtain the steady state structure of 1D shock; we run our code until the flow around the shock front reaches the steady state.

3.2.2 Dust velocity and temperature

While the gas is decelerated by shock, dust particle flows through the gas, and heated by the gas-dust collision. In the 1D steady state shock obtained above, we calculate dust velocity relative to gas. The equation of motion of dust is (Hood & Horanyi 1991)

$$\frac{4}{3}\pi\rho_{\rm mat}a_{\rm dust}^3\frac{dV_{\rm dust}}{dt} = -\pi a_{\rm dust}^2\frac{C_D}{2}\rho V_{\rm dust}^2.$$

We calculate the equation of motion by the 4th order Runge-Kutta method. The time step of the integration is set to be $0.01 \times \tau_{stop}$, where τ_{stop} is the dust stopping time defined as

$$\tau_{\rm stop} = \frac{4\rho_{\rm mat}a_{\rm dust}}{3\rho V_{\rm dust}},$$

where $\rho_{\rm mat}$, $V_{\rm dust}$, C_D are grain material density, grain velocity relative to the gas flow, and the drag coefficient, respectively. In this work, we set $\rho_{\rm mat} = 3.0$ g cm^{-3}. The drag coefficient (C_D) is given by (Hood & Horanyi 1991)

$$C_D = \frac{2}{3s_a}\left(\frac{\pi T_{\rm dust}}{T_{\rm gas}}\right) + \frac{2s_a^2+1}{s_a^3\sqrt{\pi}}\exp(-s_a^2) + \frac{4s_a^4+4s_a^2-1}{2s_a^4}{\rm erf}(s_a),$$

where $s_a = V_{\rm dust}/V_T$ is the ratio of the relative grain velocity ($V_{\rm dust}$) to the gas thermal velocity ($V_T = \sqrt{2k_{\rm bol}T_{\rm gas}/m_{\rm gas}}$).

Dust temperature is determined by the balance between heating and cooling; gas-grain energy transfer rate per dust grain (Γ_d) and cooling rate by thermal emission of dust (Λ_d):

$$\Gamma_d = 4\pi a_{\rm dust}^2\rho_{\rm gas}V_{\rm dust}(T_{\rm rec}-T_{\rm dust})C_H \tag{3.2}$$

$$\Lambda_d = 4\pi a_{\rm dust}^2\epsilon_{em}\sigma_{SB}T_{\rm dust}^4,$$

where ϵ_{em} and σ_{SB} are emission coefficient and Stefan Boltzmann constant, respectively. We adopt the emission coefficient (ϵ_{em}) of silicate model in Draine & Lee (1984) . The adiabatic recovery temperature, $T_{\rm rec}$, and the heat transfer function, C_H, are (Hood & Horanyi 1991)

$$T_{\rm rec} = \frac{T_{\rm gas}}{\gamma+1}\left(2\gamma+2(\gamma-1)s_a^2 - \frac{\gamma-1}{1/2+s_a^2+\frac{s_a}{\sqrt{\pi}{\rm erf}(s_a)}\exp(-s_a^2)}\right)$$

$$C_H = \frac{\gamma+1}{\gamma-1}\frac{k_{\rm bol}}{8m_{\rm gas}s_a^2}\left(\frac{s_a}{\sqrt{\pi}}\exp(-s_a^2) + \left(1/2+s_a^2\right){\rm erf}(s_a)\right).$$

In the limit of $V_{\rm dust} = 0$, equation (3.2) is equal to equation (3.1) (see section 2 of Hood & Horanyi 1991).

3.2.3 Sputtering and thermal evaporation

We calculate sputtering and thermal desorption of grain surface species along the flow of dust particles, using the gas and dust temperature, gas number density, and relative velocity, obtained in the previous subsection. We calculate sputtering and thermal desorption separately to investigate which is more effective to desorb grain surface species. When a dust particle of radius $a_{\rm dust}$ is moving with the velocity $V_{\rm dust}$ relative to gas, the sputtering rate of grain surface species i per unit volume is (Draine & Salpeter 1979, also see Jiménez-Serra et al. 2008)

$$\frac{dn_i}{dt} = \frac{n_i}{\sum_j n_j}\pi a_{\rm dust}^2 n_p n_{\rm dust} \int dx x^2 \left(\frac{8k_{\rm bol}T_{\rm gas}}{m_i\pi}\right)^{0.5} \frac{1}{2s}\left(e^{-(x-s)^2} - e^{-(x+s)^2}\right) \langle Y(E = x^2 k_{\rm bol}T_{\rm gas})\rangle_\theta, \tag{3.3}$$

where n_i, n_p and $n_{\rm dust}$ are the number densities of dust surface species i, projectile species and dust grain, respectively. $x^2 = \frac{1}{2}m_p v^2/k_{\rm bol}T_{\rm gas} = E/k_{\rm bol}T_{\rm gas}$ is the kinetic energy of the projectile relative to thermal energy. $\sum_j n_j$ is the summation of number density of dust surface species. The projectile impact energy relative to thermal energy of gas is $s^2 = \frac{m_p V_{\rm dust}^2}{2k_{\rm bol}T_{\rm gas}}$. The term in integral

$$\int dx x^2 \left(\frac{8k_{\rm bol}T_{\rm gas}}{m_i\pi}\right)^{0.5} \frac{1}{2s}\left(e^{-(x-s)^2} - e^{-(x+s)^2}\right)$$

is the average gas velocity relative to dust (See appendix B.1). $\langle Y(E)\rangle_\theta$ is the angle-averaged sputtering yield (Draine & Salpeter 1979)

$$< Y >_\theta = 2Y(E, \theta = 0) = 2 \times 8.3 \times 10^{-4} \frac{(\epsilon - \epsilon_0)^2}{1 + (\epsilon/30)^{\frac{4}{3}}}, \quad \epsilon > \epsilon_0,$$

$$\epsilon = \frac{\eta x^2 k_{bol} T_{\rm gas}}{E_b}$$

$$\epsilon_0 = {\rm Max}[1, 4\eta]$$

$$\eta = 4 \times \xi m_p M_t (m_p + M_t)^{-2},$$

where E_b and M_t are the binding energy and mass of the target species i. Binding energies of molecules are adopted from Garrod & Herbst (2006). ξ is 0.8 for ice and 1.0 for atoms on grain surfaces. In this work, we restrict ourselves to desorption of ice, and thus set ξ

to be 0.8. Basically, when kinetic energy of projectile is larger than $4E_b$, a projectile can sputter dust surface species (see e.g. Barlow 1978; Draine & Salpeter 1979; Draine 1995). The projectiles are gas particles of H_2, He, CO.

We calculate the thermal desorption using the following equation

$$\frac{dn_i}{dt} = n_i \nu_i \exp(-\frac{E_b}{k_{\rm bol} T_{\rm gas}}).$$

The characteristic vibrational frequency of the dust surface species i is

$$\nu_i = \sqrt{\frac{2\sigma E_b}{m_i \pi^2}},$$

where $\sigma = 1.5 \times 10^{15}$ cm^{-2} is the surface density of binding sites.

We adopt the initial abundances of dust surface species from Nomura & Millar (2004) (see Table 3.2). In this work, we assume that gas-dust mass ratio is 100:1. We also investigate desorption of molecules which are not in Table 3.2, such as SO. In that case, we set their initial abundances to be 5.0×10^{-8} relative to hydrogen (i.e. 1.8×10^{-4} relative to water ice). The relative amount of desorbed species to its initial abundance, however, does not depend on the initial abundance, as long as the abundance of the dominant ice, H_2O, is fixed (see equation (3.3)).

3.3 Results

3.3.1 sputtering

We calculated the amount of molecules desorbed via sputtering by following a dust particle in the 1D shock models. Figure 3.2 shows a model with pre-shock velocity $V_{\rm acc} = 10$ km s^{-1} and density $n_{\rm H} = 10^8$ cm^{-3}. Temperatures of gas and dust, relative velocity of dust to gas are plotted as a function of time in the coordinate of the dust particle. The moment the dust particle passes through the shock front is set to $t = 0$ in the plot. The solid line depicts the integrated amount of sputtered H_2O along the flow relative to the initial H_2O ice abundance. Although we do not plot gas density $n_{\rm H}$ in this figure, it is about 6×10^8 cm^{-3} in the post-shock (cf. Landau & Lifshitz 1987) until it increases sharply at $t \sim 0.1$ yr to keep the pressure constant as the gas cools. We can see that the dust particle is sputtered by friction between gas and dust until the dust particle is stopped

by collisions with gas at $t \sim \tau_{\rm stop} \sim 10^{-3}$ yr. We call this phase as stage 1. After stage 1, the dust particle is sputtered gradually by collisions with hot gas until gas is cooled in $t \sim \tau_{\rm cool} \sim 0.1$ yr (stage 2). If gas temperature is high, sputtering in stage 2 is effective in comparison with that in stage 1.

Figure 3.3 shows the maximum gas and dust temperature as a function of pre-shock ($V_{\rm acc}$ = 1 km s^{-1} - 10 km s^{-1}) and number density. The maximum *gas* temperature is determined by Rankin-Ugonio relations (Landau & Lifshitz 1987) and does not depend on pre-shock density. On the other hand, maximum *dust* temperature is determined by the balance between heating by collisions with gases and cooling by thermal radiation (see Appendix B.2). The dust temperature is higher when the gas density is larger, because more frequent collisions with gases lead to larger heating rate.

We calculated the amount of sputtered volatile molecules in various shock models. Figure 3.4 shows the fraction of sputtered H_2O, SO, CO_2 and CH_4 to their initial ice abundances as a function of the pre-shock velocity($V_{\rm acc}$ = 1 km s^{-1} - 10 km s^{-1}) with the fixed pre-shock density of $n_{\rm H} = 10^8$ cm^{-3}. The binding energies ($E_b/k_{\rm bol}$) of the molecules onto grain surfaces are set to be 5700 K for H_2O, 2600 K for SO, 2575 K for CO_2, and 1300 K for CH_4. For example, the fraction of sputtered H_2O is only 0.2% at 10 km s^{-1}. The sputtered fraction of SO is similar to that of CO_2, because the binding energy of SO is close to that of CO_2. We can see that volatile species like CH_4 can be sputtered completely at 10 km s^{-1}. We performed additional calculations covering higher pre-shock velocities to find that if $V_{\rm acc}$ = 19 km s^{-1}, H_2O can be completely desorbed by sputtering; 10 % of H_2O is sputtered in stage 1 and the rest is sputtered in stage 2. We speculate, however, our calculation overestimates the sputtering rate in such high velocity regime; cooling by Ly-α and H_2 emission, which are not included in our model, could be efficient. A higher pre-shock velocity $V_{\rm acc} > 19$ km s^{-1} is needed to completely desorb H_2 ice by sputtering.

Figure 3.5 shows the temporal variation of the fraction of sputtered H_2O in models with pre-shock density $n_{\rm H} = 10^8$ and 10^9 cm^{-3}. The pre-shock velocity is fixed with $V_{\rm acc}$ = 10 km s^{-1}. We can see that the total fraction of sputtered H_2O does not depend on pre-shock density, although the sputtering completes earlier in the higher density model. In stage 1, the number of desorbed species (N_i) is proportional to the product of stopping time

of dust ($\tau_{\rm stop}$) and number density ($n_{\rm H}$), i.e. $N_i \propto n_{\rm H}\tau_{\rm stop}$. Since the stopping time is proportional to $1/n_{\rm H}$, N_i is independent of $n_{\rm H}$. In stage 2, the number of desorbed species (N_i) is proportional to the product of cooling time of shocked gas ($\tau_{\rm cool}$) and number density ($n_{\rm H}$), i.e. $N_i \propto n_{\rm H}\tau_{\rm cool}$. Since the cooling time is proportional to $1/n_{\rm H}$, N_i is again independent of $n_{\rm H}$.

3.3.2 thermal evaporation

Figure 3.2 also shows the temporal variation of the fraction of thermally desorbed H_2O in the model with pre-shock $n_{\rm H} = 10^8$ cm^{-3} and $V_{\rm acc}$=10 km s^{-1}. We can see that the thermal desorption occurs right after the dust particle passes the shock front. The fraction of thermally desorbed H_2O is determined by the maximum dust temperature, which is achieved immediately after the shock front.

Figure 3.6 shows the fraction of thermally desorbed H_2O, SO, CO_2 and CH_4 as functions of the pre-shock velocity and density. The fraction of sputtered molecules is shown with the solid lines for a comparison. The thermal desorption is more effective than sputtering, because the gas number density in our work is high enough to raise the dust temperature by shock wave (see Appendix B.2). Finally, we show the critical velocity above which the species is completely desorbed (Figure 3.7). We can see that H_2O can be completely desorbed at $V_{\rm acc} = 8$ km s^{-1} if the pre-shock density $n_{\rm H}$ is 10^9 cm^{-3}. This threshold velocity is slightly lower than that obtained by Neufeld & Hollenbach (1994) ($\sim$10 km s^{-1}), because our desorption energy of H_2O is lower than their value. Except for this small shift in the critical velocity, our result is basically consistent with Neufeld & Hollenbach (1994) (see also Figure 3.7). We can also see that SO and CO_2 can be desorbed at $V_{\rm acc}$ $\sim$several km s^{-1} when $n_{\rm H} \geq 10^7$ cm^{-3}. The most volatile species CH_4 can be desorbed at lower gas density, i.e. $n_{\rm H} = 10^6$ cm^{-3}.

3.3.3 Column density of warm gas

Recent ALMA observation by Sakai et al. (2014) detected warm SO emission towards L1527. The velocity position diagram indicates that the warm SO exists in a ring region of radius $r \sim 100$ AU, which could be heated by accretion shock from the protostellar envelope

to the forming protoplanetary disk. In this subsection, we compare the temperature and column density of warm gas produced by the 1D shock with this observation. Firstly, it is useful to analytically evaluate the column density of warm gas $N_{\rm warm}$ in the shock. When the gas temperature is much higher than dust temperature, $N_{\rm warm}$ can be estimated roughly $n_{\rm pre}V_{\rm acc}\tau_{\rm cool}$, where $n_{\rm pre}$, $V_{\rm acc}$ and $\tau_{\rm cool}$ are number density of pre-shock gas, accretion velocity, and cooling time scale, respectively. The cooling time $\tau_{\rm cool}$ is

$$\tau_{cool} = p_{\rm post}/((\gamma-1)\Lambda) \sim 6 \left(\frac{a_{\rm dust}}{0.1\mu m}\right) \left(\frac{\rho_{\rm mat}}{3.0\ {\rm g\ cm^{-3}}}\right) \left(\frac{R_{gd}}{100}\right) \left(\frac{100K}{T_{\rm post}}\right)^{0.5} \left(\frac{10^8\ {\rm cm^{-3}}}{n_{\rm post}}\right)\ {\rm yr},$$

where $p_{\rm post}$, $T_{\rm post}$, $n_{\rm post}$, Λ and $R_{gd} = \rho_{\rm gas}/\rho_{\rm dust}$ are gas pressure, temperature, and number density of post-shock region, cooling rate by gas-dust collision per unit volume and time, and gas-dust mass ratio, which is typically 100 in interstellar gas (see Tielens 2005). Using the relation between the kinetic energy of the bulk motion in the pre-shock gas and thermal energy in the post-shock gas, we obtain

$$\frac{1}{2}V_{acc}^2 = \frac{p_{\rm post}}{\rho_{\rm post}(\gamma-1)} = \frac{k_{\rm bol}T_{\rm post}}{m_{\rm gas}(\gamma-1)},$$

where $m_{\rm gas}$ is the mass of a gas particle. It is straightforward to derive

$$N_{\rm warm} \sim n_{\rm pre}V_{\rm acc}\tau_{\rm cool} \sim 4.2\times10^{20} \left(\frac{a_{\rm dust}}{0.1\mu m}\right) \left(\frac{\rho_{\rm mat}}{3.0\ {\rm g\ cm^{-3}}}\right) \left(\frac{R_{gd}}{100}\right) \left(\frac{6.0}{n_{\rm post}/n_{\rm pre}}\right)\ {\rm cm^{-2}}.$$

We can see that $N_{\rm warm}$ does not depend on pre-shock gas density.

Figure 3.8 shows the column density of warm gas $N_{\rm warm}$ with temperature higher than 50, 100, 500, and 1000 K, as a function of pre-shock velocity for pre-shock densities of $n_{\rm H} = 10^7$ and 10^8 cm^{-3}. As expected from the analytical estimate, $N_{\rm warm}$ is of order 10^{21} cm^{-2} or less.

The radial size of the SO ring around L1527 is about 100 AU. The free-fall velocity at this distance is about 3 km s^{-1}, considering the estimated mass of the central object (0.5 $M_{\rm sun}$)(Tobin et al. 2013). The gas density in the envelope is not well constrained from the observation, but the density of $\gtrsim 10^7$ cm^{-3} is consistent with the model of L1527 by Tobin et al. (2013). Our 1D shock model shows that the desorption of SO is possible with $V_{\rm acc} = 3$ km s^{-1} and $n_{\rm H} \gtrsim 10^8$ cm^{-3}. With this parameter set, the column density of warm gas $T > 100$ is $\sim 1\times10^{21}$ cm^{-2}. Sakai et al. (2014) derived SO temperature ~ 70 K

and column density $\sim 10^{14}$ cm^{-2}. We can conclude that the SO emission around L1527 is consistent with the 1D J-shock. According to the chemical model of protostellar core (e.g. Wakelam et al. 2011; Aikawa et al. 2012), SO ice is one of the major carrier of sulfur; desorption of SO ice of abundance $\sim 10^{-7}$ at the shock is fairly reasonable.

The molecules with higher desorption energies such as H_2O, and CH_3OH are difficult to desorb with $V_{acc} \sim 3$ km s^{-1}. In our model, CO_2, C_2H_2, CCS, CH_2PH, CH_3CHO, H_2CN, H_2CS, H_2S, NO_2, and OCN have similar desorption energies to SO. They could be detected in the SO ring, if they are abundant in the ice in the protostellar envelope.

3.4 Summary

In this work, we calculate the desorption of dust surface species by sputtering and thermal desorption in 1D shock with pre-shock gas density $n_H = 10^6 - 10^9$ cm^{-3} and velocity $1 - 10$ km s^{-1}. We compare our results with the recent observation of warm SO emission towards young protostellar core to investigate if such emission could originate in accretion shock onto a forming protoplanetary disk. Our findings are as follows

- Thermal desorption is more effective than sputtering in the accretion shock of protoplanetary disk, because of the high gas density.
- We derived parameter regime of gas density and velocity, with which volatiles, H_2O, SO, CO_2 and CH_4 can be desorbed to the gas phase. For example, thermal desorption can desorb H_2O in the shock with $V_{acc} \geq 8$ km s^{-1} if the gas density is higher than $n_H = 10^9$ cm^{-3}, while sputtering is negligible at $V_{acc} \lesssim 10$ km s^{-1} .
- We show the column density of warm gas $\gtrsim 100$ K in the post-shock region is $\sim 10^{21}$ cm^{-2}. The value only weakly depends on the pre-shock density and velocity, as long as the gas-dust collision is the main cooling mechanism in the post-shock gas.
- The temperature and column density of SO estimated from the observation are consistent with the accretion shock from the envelope onto the forming protoplanetary disk.

$n_{\rm H}$ ($\rm cm^{-3}$)	L_{cal}(pc)
10^6	1.0×10^{-3}
10^7	1.5×10^{-4}
10^8	2.5×10^{-5}
10^9	2.0×10^{-6}

Table 3.1: Model parameter

Species	Abundance	Species	Abundance
H_2	0.5	H_2S	1.0×10^{-7}
He	0.1	OCS	5.0×10^{-8}
H_2O	2.8×10^{-4}	Si	3.6×10^{-8}
CO	1.3×10^{-4}	PH_3	1.2×10^{-8}
H	5.0×10^{-5}	S	5.0×10^{-9}
N_2	3.7×10^{-5}	C_2H_4	5.0×10^{-9}
CO_2	3.0×10^{-6}	C_2H_5OH	5.0×10^{-9}
H_2CO	2.0×10^{-6}	C_2H_6	5.0×10^{-9}
O_2	1.0×10^{-6}	Fe^+	2.4×10^{-8}
NH_3	6.0×10^{-7}	H_3^+	1.0×10^{-9}
C_2H_2	5.0×10^{-7}	H^+	1.0×10^{-11}
CH_4	2.0×10^{-7}	He^+	2.5×10^{-12}
CH_3OH	2.0×10^{-7}		

Table 3.2: Initial molecular abundances relative to hydrogen nuclei

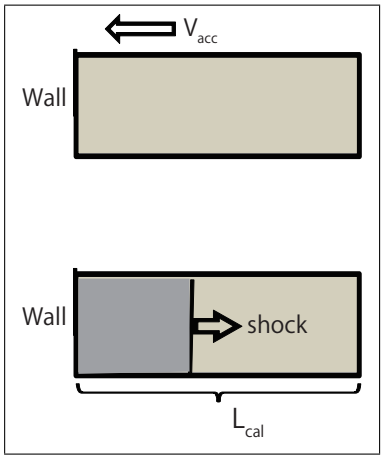

Figure 3.1: Schematic view of our 1D shock model

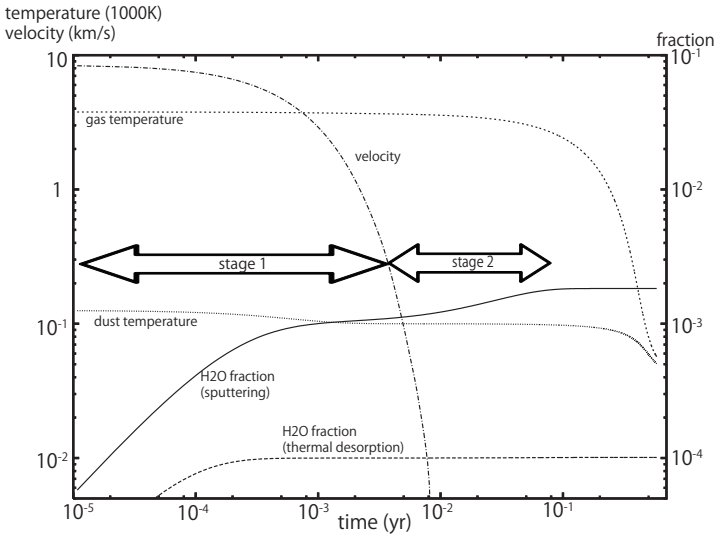

Figure 3.2: Temporal variations of fractional abundance of sputtered H_2O by sputtering and thermal desorption, gas and dust temperature, and dust velocity (km s^{-1}) relative to gas flow in the coordinate of the dust particle in the model with pre-shock velocity and density of $V_{\rm acc}$ =10km s^{-1} and $n_{\rm H} = 10^8$ cm^{-3}.

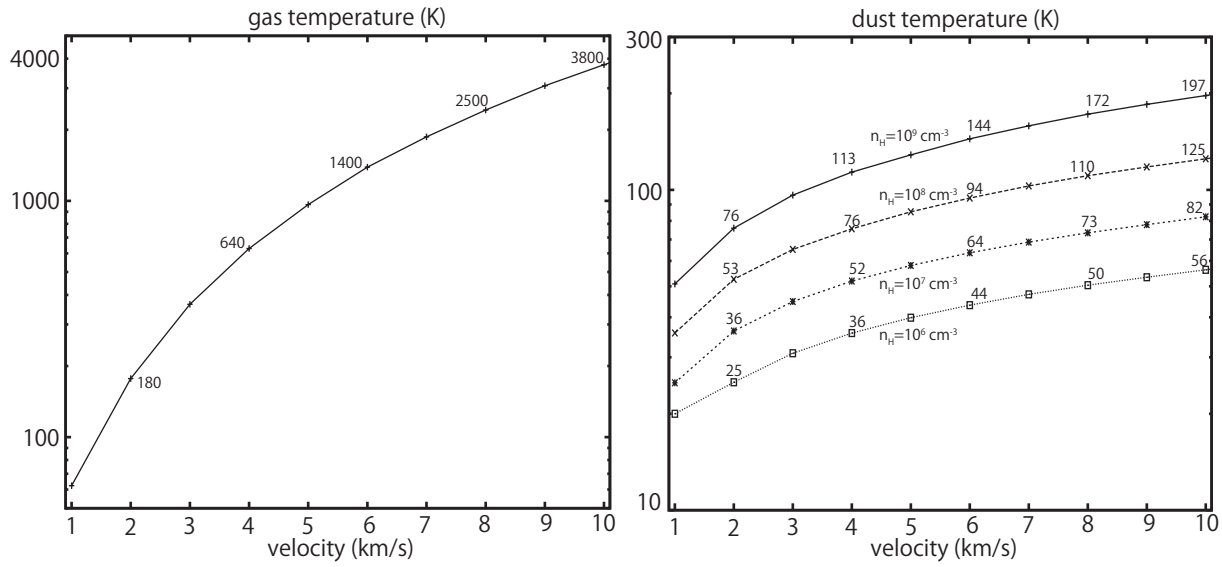

Figure 3.3: Max gas temperature (left) and max dust temperature (right) as a function of pre-shock velocity. The values of the vertical axis (gas or dust temperature) are labeled on some points.

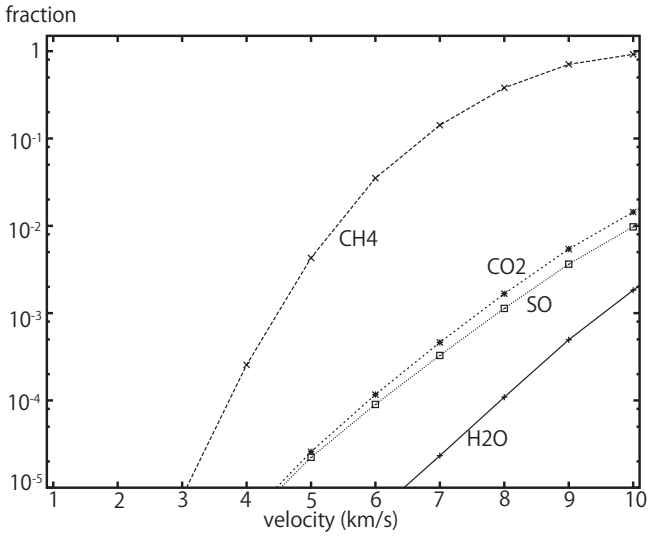

Figure 3.4: The fraction of sputtered H_2O, SO, CO_2, and CH_4 to their initial ice abundances as a function of the pre-shock velocity. The pre-shock density is fixed with $n_{\rm H} = 10^8$ cm^{-3}.

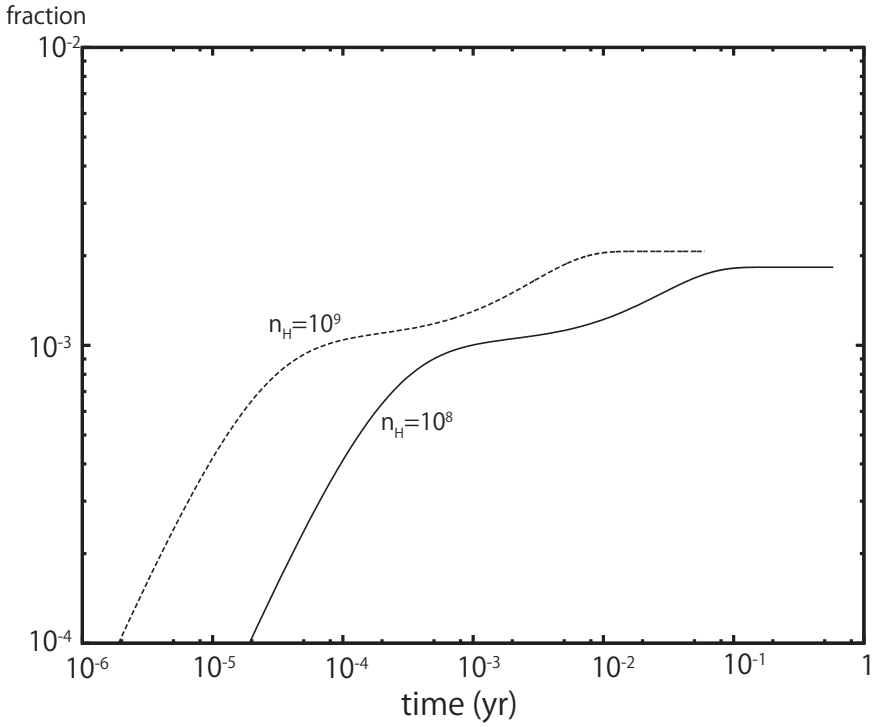

Figure 3.5: Temporal variations of fractional abundance of sputtered H_2O at $n_{\rm H} = 10^8$ and $n_{\rm H} = 10^9$ cm^{-3}. The pre-shock velocity is fixed with $V_{\rm acc} = 10$ km s^{-1}.

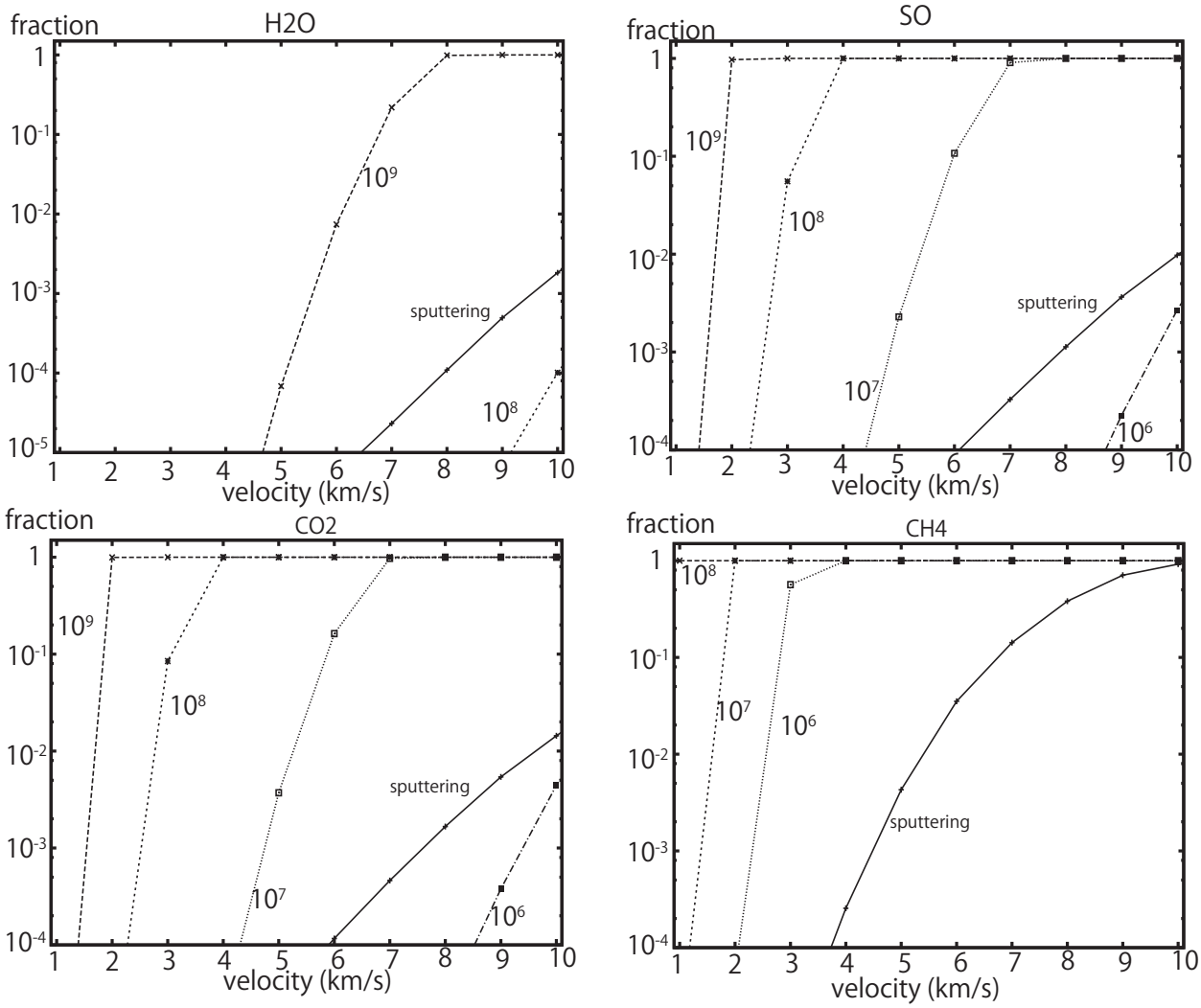

Figure 3.6: Fractional abundance of thermally desorbed and sputtered H_2O, SO, CO_2, and CH_4 as a function of pre-shock velocity (1-10km s^{-1}) with number density $n_H = 10^6, 10^7, 10^8$, and 10^9 cm^{-3}.

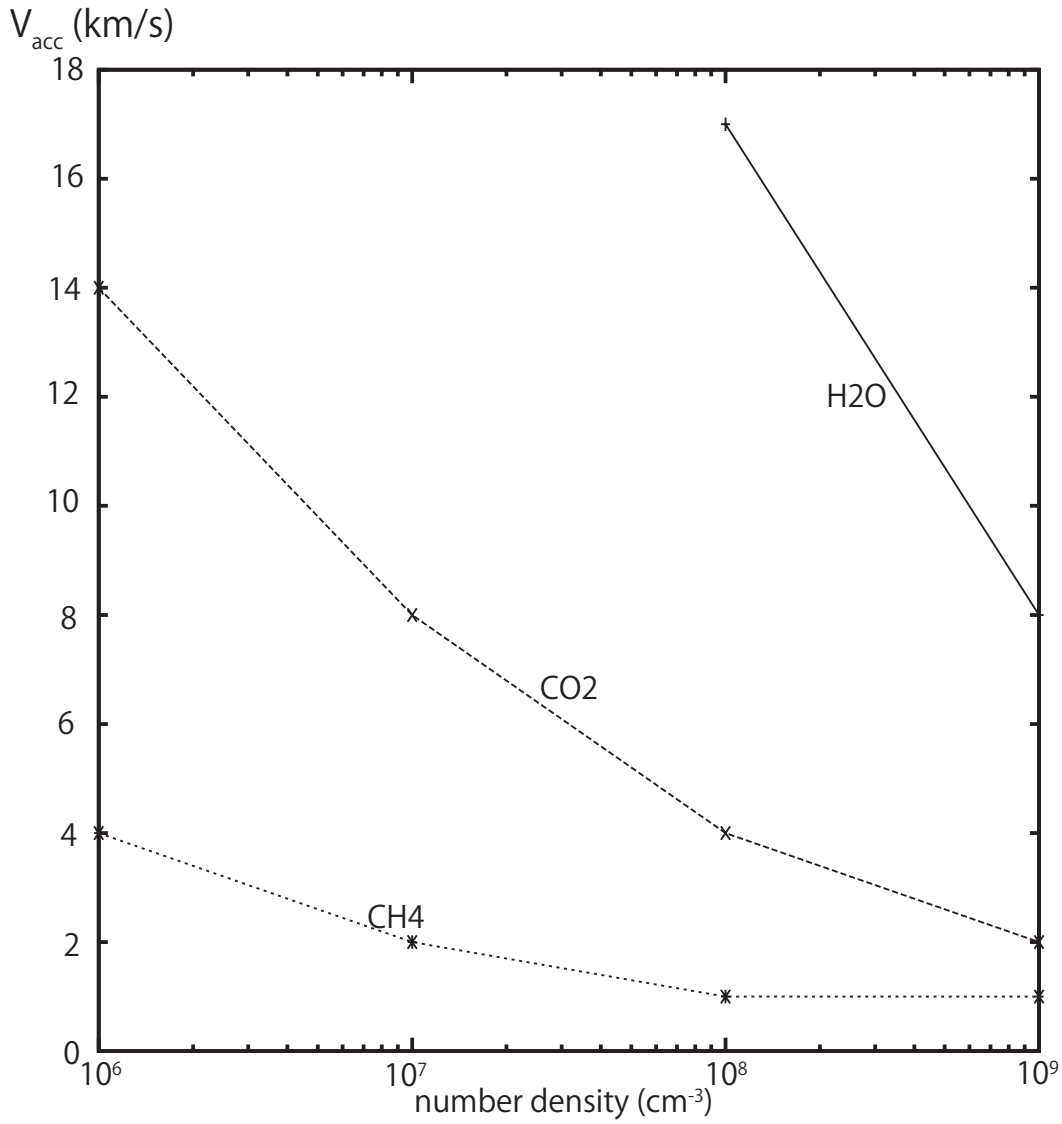

Figure 3.7: Critical velocity above which H_2O, SO, CO_2 and CH_4 are completely desorbed as a function of pre-shock density. Critical velocity of SO is almost the same as that of CO_2.

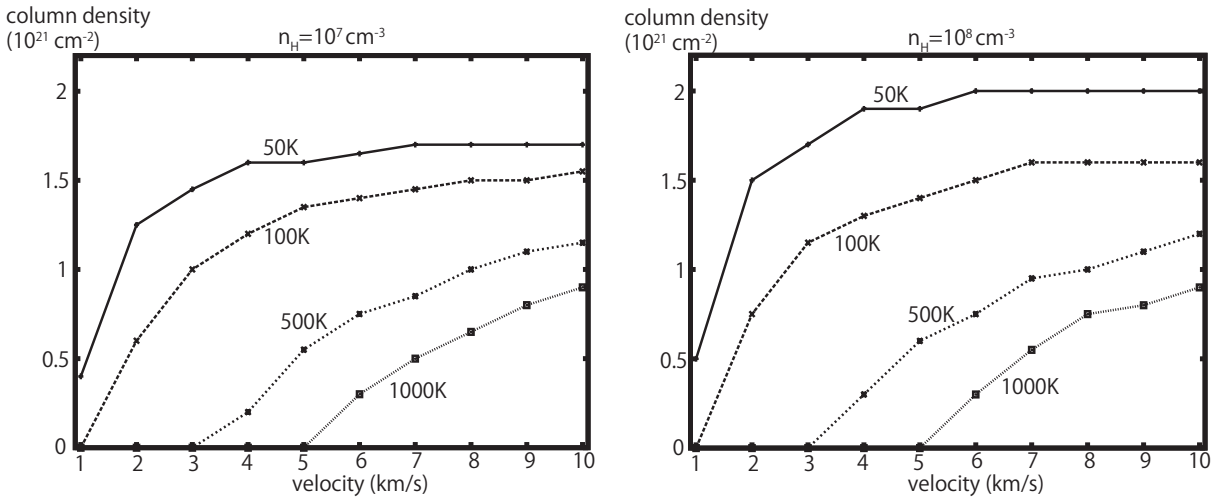

Figure 3.8: Column density of post-shock gas warmer than 50, 100, 500, 1000K, as a function of pre-shock velocity ($V_{\rm acc}$) with pre-shock density ($n_{\rm H}$) of 10^7 (left) and 10^8 cm^{-3} (right).

Appendix A

Appendix of Chapter 1

A.1 Modification of Balbus criterion

We assume a gas with the cooling rate $An^{\beta}T^{\gamma}$ (cf. Elmegreen 1991 Elmegreen (1991)). The number density and temperature of an unperturbed state are n_0 and T_0. Then the gas is compressed isobarically; the perturbed gas density and temperatures are $n_p = \alpha n_0$ ($\alpha > 1$) and $T_p = T_0/\alpha$. Balbus criterion becomes

$$\frac{\partial}{\partial T}\left(\frac{\Lambda - \Gamma}{T}\right)_p \simeq \frac{AT_p^{\gamma} n_p^{\beta}/T_p - AT_0^{\gamma} n_0^{\beta}/T_0}{T_p - T_0} < 0. \tag{A.1}$$

Considering $T_p - T_0 < 0$, $n_p = \alpha n_0$ and $T_p = T_0/\alpha$, it is straightforward to derive

$$AT_p^{\gamma} n_p^{\beta}/T_p - AT_0^{\gamma} n_0^{\beta}/T_0 = AT_0^{\gamma-1} n_0^{\beta}\left(\alpha^{\beta-\gamma+1} - 1\right) > 0. \tag{A.2}$$

We can see that the Balbus criterion is satisfied if $\beta - \gamma + 1 > 0$.

A.2 Temperature dependence of dust-gas collisional cooling

The cooling function of dust-gas collisional cooling is

$$f[T] = AT^{0.5}\left(T - T_{\rm dust}\right), \tag{A.3}$$

where A is constant, and T and $T_{\rm dust}$ are temperatures of gas and dust, respectively. The power index $\gamma = \partial \ln(f[T])/\partial \ln(T)$ becomes

$$\gamma \simeq \frac{\ln(f[(1+d\delta)T]) - \ln(f[T])}{\ln((1+d\delta)T) - \ln(T)}, \tag{A.4}$$

where $d\delta \simeq 0$. We set $T = \alpha T_{\rm dust}$, and it is straightforward to derive

$$\gamma \simeq 0.5 + \frac{\ln(1 + d\delta(1 - 1/\alpha)^{-1})}{\ln(1 + d\delta)}. \tag{A.5}$$

If $\alpha >> 1 (T >> T_{\rm dust})$, $\gamma \simeq 1.5$ and if $\alpha \simeq 1 (T \simeq T_{\rm dust})$, γ becomes larger than 1.5.

Appendix B

Appendix of Chapter 3

B.1 Derivation of mean velocity of Draine & Salpeter (1979) formula

We consider a spherical dust with radius $a_{\rm dust}$ moving in z direction with velocity V relative to gas. Using the Maxwellian velocity distribution function at the coordinate system of dust, mean gas velocity can be expressed as

$$\int v \left(\frac{m_{\rm gas}}{2\pi k_{\rm bol} T_{\rm gas}}\right)^{3/2} \exp\left(-\frac{m_{\rm gas}}{2k_{\rm bol}T_{\rm gas}}(v_x^2+v_y^2+(v_z-V)^2)\right) dv\ v\ d\theta\ v\ \sin\theta\ d\phi.$$

θ and ϕ are polar and azimuthal angle in the velocity space (v_x, v_y, v_z). $v^2 = v_x^2 + v_y^2 + v_z^2$, $v_z = v\cos\theta$, $x = v/\sqrt{2k_{\rm bol}T_{\rm gas}/m_{\rm gas}}$, $s = V/\sqrt{2k_{\rm bol}T_{\rm gas}/m_{\rm gas}}$ and integrating ϕ $(0 \to 2\pi)$ and θ ($0 \to \pi$), it is straightforward to derive the mean velocity

$$\int dx\ x^2 \left(\frac{8m_{\rm gas}T_{\rm gas}}{\pi k_{\rm bol}}\right)^{1/2} \frac{1}{2s}\left(e^{-(x-s)^2} - e^{-(x+s)^2}\right).$$

B.2 Dust temperature

We consider a spherical dust with radius $a_{\rm dust}$ moving with velocity v relative to gas of number density $n_{\rm gas}$. When the dust collides to a gas particle, the kinetic energy of a gas particle is $\frac{1}{2}m_p v^2$, where m_p is mass of gas particle. Collision frequency of a dust particle with gas per unit time is $\pi a_{\rm dust}^2 v n_{\rm gas}$. The dust is cooled by thermal radiation $\epsilon\sigma_{SB}T_{\rm dust}^4$ per unit time and unit surface area. We assume that dust is in thermal equilibrium, which means heating rate is equal to cooling rate

$$\pi a_{\rm dust}^2 v n_{\rm gas}\left(\frac{1}{2}m_p v^2\right) = 4\pi a_{\rm dust}^2 \epsilon\sigma_{SB}T_{\rm dust}^4.$$

We set $\epsilon \sim 10^{-6}T^2$ at $a_{\rm dust} = 0.1\mu m$ (Draine & Lee 1984; Tielens 2005). For simplicity, we assume all gas particle is hydrogen molecules (H_2), which means $m_p = 3.34 \times 10^{-24}$ g and $n_{\rm gas} = n_{H_2}$. It is straightforward to derive

$$T_{\rm dust} \sim 1.4 \left(\frac{v}{1km/s} \right)^{0.5} n_{H_2}^{1/6}.$$

We can see that it is difficult to raise the dust temperature by shock when the number density of gas is low; i.e. $n_{H_2} < 10^6$ cm^{-3}.

Bibliography

Agúndez, M., Cernicharo, J., & Guélin, M. 2007, ApJ, 662, L91

Agúndez, M., Cernicharo, J., Pardo, J.R., Guélin, M. & Philips, T.G. 2008. A&A, 485, L33

Aikawa, Y., Ohashi, N., Inutsuka, S., Herbst, E., Takakuwa, S. 2001 ApJ, 552, 639

Aikawa, Y., Wakelam, V., Garrod, R. T., & Herbst, E. 2008, ApJ, 674, 984

Aikawa, Y., Wakelam, V., Hersant, F., Garrod, R. T., & Herbst, E. 2012, ApJ, 760, 40

Adams, N.G., McIntosh, B.J., Smith, D. 1990, A&A, 232, 443

Arce, H.G., Santiago-García, J., Jorgensen,J.K., Tafalla, M., Bachiller R. 2008, ApJ, 681, 21

Asplund, M., Grevesse, N., Sauval, A. J., & Scott, P. 2009, ARA&A, 47,481

Bachiller,R., & Pérez Gutiérrez, M. 1997, ApJ, 487, 93

Bakes, E.L.O., & Tielens, A.G.G.M. 1994 ApJ, 427, 822

Balbus, S.A. 1986, ApJ, 303, L79

Banerjee, R., Vázquez-Semadeni, E., Hennebelle, P., & Klessen, R.S. 2009, MNRAS, 398, 1082

Barlow, M. J. 1978, MNRAS, 183, 367

Benedettini, M., Busquet, G., Lefloch, B. et al. 2012, A&A, 539, L3

Bergin, E. A., Neufeld, D. A., & Melnick, G. J. 1998, ApJ, 499, 777

Bergin, E. A., Neufeld, D. A., & Melnick, G. J. 1999, ApJ, 510, 145

Bergin, E. A., Hartmann, L. W., Raymond, J. C., & Ballesteros-Paredes, J. 2004, ApJ, 612, 921

Black, J.H., & Dalgarno, A. 1977, ApJS, 34, 405

Boley, A. C., Mejia, A. C. Durisen, R. H., et al. 2006, ApJ, 651, 517

Boley, A. C., & Durisen, R. H. 2008, ApJ, 685, 1193

Boss, A. P. 2008, ApJ, 677, 607

Caselli, P., Hartquist, T.W., & Havnes, O. 1997, A&A, 322, 296

Charnley, S.B., & Millar, T.J. 1994, MNRAS, 270, 570

Clark, P. C., Glover, S. C. O., Klessen, R. S., & Bonnell, I. A. 2012, MNRAS, 424, 2599

Davis, C. J., & Eisloeffel, J. 1995, A&A, 300, 851

de Jong, T., Dalgarno, A., & Boland, W. 1980, A&A, 91, 68

Draine, B. T. 1980, ApJ, 241, 1021

Draine, B. T. 1995, Ap&SS, 233, 111

Draine, B. T., & Lee, H. M. 1984, ApJ, 285, 89

Draine, B.T., Roberge, W.G., Dalgarno, A. 1983, ApJ, 246, 485

Draine, B. T. & Salpeter, E. E. 1979, ApJ, 231, 77

Elmegreen, B.G. 1991, in The Physics of Star Formation and Early Stellar Evolution, ed. C.J. Lada & N. D. Kylafis (NATO ASI Ser. C, 342; Dordrecht:Kluwer), 35

Elmegreen, B.G., & Scalo, J. 2004, ARA&A, 42, 211

Field, G.B. 1965, ApJ, 142, 531

Field, G.B., Goldsmith, D.W., & Habing, H.J. 1969, ApJ, 155, L149

Flower, D.R., Pineau des Forets, G., & Hartquist, T.W. 1985, MNRAS, 216, 775

Flower, D.R., Pineau des Forets, G., Field, D., & May, P.W. 1996, MNRAS, 280, 447

Flower, D.R., & Pineau des Forets, G. 2010, MNRAS, 406, 1745

Frost, M. J., Sharkey, P., & Smith, I. W. M. 1993, J. Phys. Chem., 97, 12254

Fukui, Y., Kawamura, A., Minamidani, T. et al. 2008, ApJS, 178, 56

Furuya, K., Aikawa, Y., Tomida, K. et al. 2012, ApJ, 758, 86

Furuya, K., Aikawa, Y., Nomura, H., Hersant, F., & Wakelam, V. 2013, ApJ, 779, 11

Garrod, R.T., & Herbst, E., 2006, A&A, 457, 927

Gilden, D.L. 1984, ApJ, 283, 679

Glassgold, A.E., & Langer, W.D. 1975, ApJ, 197, 347

Glassgold, A.E., & Langer, W.D. 1976, ApJ, 204, 403

Glover, S.C.O., & Mac Low, M-M. 2007, ApJS, 169, 239

Glover, S. C. O., & Mac Low, M-M. 2007, ApJ, 659, 1317

Glover, S. C. O., Federrath, C., Mac Low, M.-M., & Klessen, R. S. 2010, MNRAS, 404, 2

Goldsmith, P.F., & Langer, W.D. 1978, ApJ, 222, 881

Guélin, M., Cernicharo, J., Paubert, G., & Turner, B. E. 1990, A&A 230, L9

Gusdorf, A., Cabrit, S., Flower, D.R., Pineau des Forets, G. 2008, A&A 482, 809

Habing, H.J. 1968, Bull. Astron. Inst. Netherlands, 19, 421

Halfen, D.T., Clouthier, D.J., & Ziurys, L.M. 2008, ApJ, 677, L101

Harada, N., Herbst, E. & Wakelam, V., 2010, ApJ, 721, 1570

Harada, N., Herbst, E. & Wakelam, V., 2012, ApJ, 756, 104

Hartmann L., Accretion Processes in Star Formation, 1998, Cambridge University Press

Hassel, G. E., Herbst, E., & Bergin, E. A. 2010, A&A, 515, 66

Heiles, C. 1997, ApJ, 481, 193

Heiles, C., & Troland, T.H. 2003, ApJ, 586, 1067

Heiles, C., & Troland, T.H. 2005, ApJ, 624, 773

Heinzeller, D.; Nomura, H.; Walsh, C., & Millar, T. J. 2011, ApJ, 731, 115

Heithausen, A. 2002, A&A, 393, L41

Heitsch, F., Burkert, A., Hartmann, L.W., Slyz, A.D., & Devriendt, J.E.G. 2005, ApJ, 633, L113

Heitsch, F., Hartmann, L.W., Slyz, A.D., Devriendt, J.E.G., & Burkert, A. 2008, ApJ, 674, 316

Hennebelle, P., & Audit, E. 2007, A&A, 465, 431

Hennebelle, P., & Falgarone, E. 2012, A&ARv, 20, 55

Hennebelle, P., & Pérault, M. 1999, A&A, 351, 309

Herbst, E., & Van Dishoeck, E. F. 2009, ARA&A, 47, 427

Hersant, F., Wakelam, V., Dutrey, A., Guilloteau, S., & Herbst, E. 2009, A&A, 493, L49

Heyer, M.H., & Brunt, C.M. 2004, ApJ, 615, L45

Hirano, N., & Taniguchi, Y. 2001, ApJ, 550, L219

Hollenbach, D., & McKee, C.F. 1979, ApJS, 41, 555

Hollenbach, D., & McKee, C. F. 1980, ApJ, 241L, 47

Hollenbach, D., & McKee, C.F. 1989, ApJ, 342, 306

Hood, L. L., & Horanyi, M. 1991, Icarus, 93, 259

Hosokawa, T., & Inutsuka, S. 2006, ApJ, 646, 240

Iglesias, E. R., & Silk, J. 1978, ApJ, 226, 851

Ilee, J. D., Boley, A. C., Caselli, P., et al. 2011, MNRAS, 417, 2950

Inoue, T. & Inutsuka, S. 2008, ApJ, 687, 303

Inoue, T. & Inutsuka, S. 2009, ApJ, 704, 161

Inoue, T. & Inutsuka, S. 2012, ApJ, 759, 35

Inoue, T., Inutsuka, S., & Koyama, H. 2007, ApJ, 658, L99

Jiménez-Serra, I., Martín-Pintado, J., Rodríguez-Franco, A., & Marcelino, N. 2004, ApJ, 603, 49

Jiménez-Serra, I., Caselli,P., Martín-Pintado, J.,Hartquist,T.W. 2008, A&A, 482, 549

Koyama, H. & Inutsuka, S. 2000, ApJ, 532, 980

Koyama, H. & Inutsuka, S. 2002, ApJ, 564, L97

Kwan, J. H. 1977, ApJ, 216, 713

Landau, L. D. & Lifshitz, E.M. 1987, Fluid Mechanics, (Oxford; Butterworth-Heinemann)

Langer, W.D., Velusamy, T., Kuiper, T.B.H. et al. 1995, ApJ, 453, 293

Larson, R.B. 1981, MNRAS, 194, 809

Lee, H.-H., Herbst, E., Pineau des Foréts, G., Roueff, E., & Le Bourlot, J. 1996, A&A, 311, 690

Lunine, J. I., Engel, S, Rizk, B., & Horanyi, M. 1991, Icarus, 94, 333

Mac Low, M-M., & Klessen, R.S. 2004, Rev.Mod.Phys., 76, 125

Maret, S., Bergin, E.A., & Lada, C.J. 2006, nature, 442, 425

Mathis, J.S., Mezger, P.G., & Panagia, N. 1983, A&A, 128, 212

Matthews, H.E., Feldman, P.A., Bernath, P.F. 1987, ApJ, 312, 358

McKee, C.F., Storey, J.W.V., Watson, D.M., & Green, S. 1982, ApJ, 259, 647

Mikami, H., Umemoto, T., Yamamoto, S., & Saito, S. 1992, ApJ, 392, 87

Millar, T.J., Bennett, A., Herbst, E. 1987, MNRAS, 229, P41

Millar, T.J., Rawlings, J.M.C., Bennett, A., Brown, P.D., Charnley, S.B. 1991, A&AS, 87, 585

Moriarty-Schieven, G.H., & Snell, R.L. 1988, ApJ, 332, 364

Mumma, M. J. & Charnley, S. B. 2011, ARA&A, 49, 471

Muto, T., Grady, C. A., Hashimoto, J. et al. 2012, ApJ, 748, 22

Nadeau, D., & Geballe, T. R. 1979, ApJ, 230, 169

Nejad-Asghar, M. 2007, MNRAS, 379, 222

Nejad-Asghar, M. 2011, MNRAS, 414, 470

Neufeld, D. A., & Dalgarno, A. 1989, ApJ, 340, 869

Neufeld, D.A., & Hollenbach, D. J. 1994, ApJ, 428, 170

Nisini, B., Benedettini, M., Codella, C., et al. 2010, A&A, 518, 120

Nomura, H. & Millar, T.J. 2004, A&A, 414, 409

Parker, E.N. 1953, ApJ, 117, 431

Pineda, J. E., Maury, A. J., Fuller, G. A., et al. 2012, A&A, 544, 7

Rodgers, S. D., & Charnley, S. B. 2003, ApJ, 585, 355

Sakamoto, S., & Sunada, K. 2003, ApJ, 594, 340

Schwarz, J., McCray, R., & Stein, R.F. 1972, ApJ, 175, 673

Smith, I. W. M. 1988, MNRAS, 234, 1059

Smith, I.W.M., Herbst, E., Chang, Q. 2004, MNRAS, 350, 323

Solomon, P.M., Rivolo, A.R., Barrett, J., & Yahil, A. 1987, ApJ, 319, 730

Spitzer, L. 1978, Physical Processes in the Interstellar Medium (New York:Wiley)

Stanimirović, S., & Heiles, C. 2005, ApJ, 631, 371

Sugimura, M., Yamaguchi, T., Sakai, T., et al. 2011, PASJ, 63, 459

Tachihara, K., Saigo, K., Higuchi, A. et al. 2012, ApJ, 754, 95

Tenenbaum, E.D., Woolf, N.J., & Ziurys, L. M. 2007, ApJ, 669, L29

Thorne, L.R., Anicich, V.G., Huntress, W.T. 1983, Chem. Phys. Letters, 98, 162

Thorne, L.R., Anicich, V.G., Prasad, S.S., Huntress, W.T. 1984, ApJ, 280, 139

Tielens, A.G.G.M. 2005, The Physics and Chemistry of the Interstellar Medium (Cambridge University Press)

Tielens, A.G.G.M., & Hollenbach, D. 1985, ApJ, 291, 722

Tobin, J. J., Hartmann, L., Chiang, H-F. et al. 2013, ApJ, 771, 48

Tsukamoto, Y., Machida, M. N. & Inutsuka, S. 2013, MNRAS.436, 1667

Turner, B.E., & Bally, J. 1987, ApJ, 321, 75

Turner, B.E., Tsuji, T., Bally, J., Guelin, M., Cernichago, J. 1990, ApJ, 365, 569

Umemoto, T., Iwata, T., Fukui, Y. et al. 1992, ApJ, 392, 83

Vázquez-Semadeni, E., Gómez, G.C., Jappsen, A.K. et al. 2007, ApJ 657, 870

Vázquez-Semadeni, E., Ryu, D., Passot, T., González, R.F., & Gazol, A. 2006, ApJ 643, 245

Van Leer, B. 1979, J. Comput. Phys., 32, 101

Visser, R., van Dishoeck, E. F., Doty, S. D., & Dullemond, C. P. 2009, A&A, 495, 881

Visser, R., Doty, S. D., & van Dishoeck, E. F. 2011, A&A, 534,132

Viti, S., Jimenez-Serra, I., Yates, J.A. et al. 2011, ApJ, 740, L3

Wakelam, V., Hersant, F., & Herpin, F. 2011, A&A, 529, 112

Walsh, C., Millar, T. J., & Nomura, H. 2010, ApJ, 722, 1607

Walsh, C., Nomura, H., Millar, T. J., & Aikawa, Y. 2012, ApJ, 747, 114

Walsh, C., Millar, T. J., & Nomura, H. 2013, ApJ, 766, 23

Willacy, K. 2007, ApJ, 660, 441

Willacy, K., Klahr, H.H., Millar, T.J., Henning, Th. 1998, A&A, 338, 995

Wolfire, M.G., Hollenbach, D., McKee, C.F., Tielens, A.G.G.M. & Bakes, E.L.O. 1995, ApJ, 443, 152

Wolfire, M.G., McKee, C.F., Hollenbach, D., & Tielens, A.G.G.M. 2003, ApJ, 587, 278

Yamaguchi, T., Takano, S., Sakai, N. et al. 2011, PASJ, 63, 37

Zapata, L. A., Loinard, L., Rodriguez, L. F. et al. 2013, ApJ, 764, 14

Zel'dovich, Ya. B. & Raizer, Yu. P. 2002, Physics of Shock Waves and High-Temperature Hydrodynamic Phenomena, (N.Y; Dover Publications)

謝辞

本研究を行うにあたって、様々な方にお世話になりました。

相川祐理準教授には担当教官としてきめ細やかな指導をして頂きました。なかなか論文作成が進まず、その他様々な面で迷惑をおかけしてしまいました。私自身、決して出来がいいとは言えない学生でしたが、それでも暖かく見守って下さいました。この場をお借りして深く感謝申し上げます。

また、本研究を行うにあたり、磁気流体プログラムを提供して下さり、さらに研究を進めていくに当たり、様々なアドバイスを頂きました青山学院大学の井上剛志助教にお礼申し上げます。研究や論文作成など、色々とご迷惑をおかけしてしまいましたが、そんな中でも暖かくアドバイスを頂きました。御蔭で無事論文を完成させることができました。

宇宙物理学研究室の中川義次教授、大槻圭史教授に感謝申し上げます。研究室セミナーでの私の拙い発表の中でも暖かく様々な助言を頂きました。さらに研究室の先輩、同級生、後輩には様々な面でお世話になりました。特に、同級生である末次竜さん、古家健次さん、安井佑貴さんには研究面を初め、大変お世話になりました。全員そろって卒業できることを大変嬉しく思います。

日々お世話になっている家族に感謝申し上げます。博士進学を許していただいた御蔭で、有意義な三年間を過ごすことができました。いつも帰りが遅くなり、その他色々と心配をかけてきた三年間ですが、無事、博士論文を仕上げることができました。

本論文の第二章を執筆するにあたり、東京大学の山本智教授と山口貴弘さんからは発表前の観測結果の結果を提供して頂きました。この場をお借りしてお礼申し上げます。

本論文の副査を担当して下さり、さらに有益なコメントを頂きました中川義次教授、林祥介教授、東京大学の山本智教授に感謝申し上げます。

最後に、この三年間でお世話になった方々へ感謝申し上げます。本当にありがとうございました。